

Report Prepared by:

**Enrique A. Paz
Alberto A. Sagüés**

FINAL REPORT

**MSE Wall Void Repair Effect on Corrosion of
Reinforcement – Phase 2: Specialty Fill Materials**

**Contract No. BDV25-977-07
Final Report to Florida Department of Transportation**

**A. A. Sagüés
Principal Investigator
Department of Civil and Environmental Engineering**



**UNIVERSITY OF
SOUTH FLORIDA**

COLLEGE OF ENGINEERING

Tampa, FL 33620
August, 2015

DISCLAIMER

The opinions, findings, and conclusions expressed in this publication are those of the authors and not necessarily those of the State of Florida Department of Transportation.

UNIVERSAL CONVERSION TABLE

| SI* (MODERN METRIC) CONVERSION FACTORS | | | | |
|--|-----------------------------|-----------------------------|-----------------------------|---------------------|
| APPROXIMATE CONVERSIONS TO SI UNITS | | | | |
| Symbol | When You Know | Multiply By | To Find | Symbol |
| LENGTH | | | | |
| in | inches | 25.4 | millimeters | mm |
| ft | feet | 0.305 | meters | m |
| yd | yards | 0.914 | meters | m |
| mi | miles | 1.61 | kilometers | km |
| AREA | | | | |
| in ² | square inches | 645.2 | square millimeters | mm ² |
| ft ² | square feet | 0.093 | square meters | m ² |
| yd ² | square yard | 0.836 | square meters | m ² |
| ac | acres | 0.405 | hectares | ha |
| mi ² | square miles | 2.59 | square kilometers | km ² |
| VOLUME | | | | |
| fl oz | fluid ounces | 29.57 | milliliters | mL |
| gal | gallons | 3.785 | liters | L |
| ft ³ | cubic feet | 0.028 | cubic meters | m ³ |
| yd ³ | cubic yards | 0.765 | cubic meters | m ³ |
| NOTE: volumes greater than 1000 L shall be shown in m ³ | | | | |
| MASS | | | | |
| oz | ounces | 28.35 | grams | g |
| lb | pounds | 0.454 | kilograms | kg |
| T | short tons (2000 lb) | 0.907 | megagrams (or "metric ton") | Mg (or "t") |
| TEMPERATURE (exact degrees) | | | | |
| °F | Fahrenheit | 5 (F-32)/9 or (F-32)/1.8 | Celsius | °C |
| ILLUMINATION | | | | |
| fc | foot-candles | 10.76 | lux | lx |
| fl | foot-Lamberts | 3.426 | candela/m ² | cd/m ² |
| FORCE and PRESSURE or STRESS | | | | |
| lbf | poundforce | 4.45 | newtons | N |
| lbf/in ² | poundforce per square inch | 6.89 | kilopascals | kPa |
| APPROXIMATE CONVERSIONS FROM SI UNITS | | | | |
| Symbol | When You Know | Multiply By | To Find | Symbol |
| LENGTH | | | | |
| mm | millimeters | 0.039 | inches | in |
| m | meters | 3.28 | feet | ft |
| m | meters | 1.09 | yards | yd |
| km | kilometers | 0.621 | miles | mi |
| AREA | | | | |
| mm ² | square millimeters | 0.0016 | square inches | in ² |
| m ² | square meters | 10.764 | square feet | ft ² |
| m ² | square meters | 1.195 | square yards | yd ² |
| ha | hectares | 2.47 | acres | ac |
| km ² | square kilometers | 0.386 | square miles | mi ² |
| VOLUME | | | | |
| mL | milliliters | 0.034 | fluid ounces | fl oz |
| L | liters | 0.264 | gallons | gal |
| m ³ | cubic meters | 35.314 | cubic feet | ft ³ |
| m ³ | cubic meters | 1.307 | cubic yards | yd ³ |
| MASS | | | | |
| g | grams | 0.035 | ounces | oz |
| kg | kilograms | 2.202 | pounds | lb |
| Mg (or "t") | megagrams (or "metric ton") | 1.103 | short tons (2000 lb) | T |
| TEMPERATURE (exact degrees) | | | | |
| °C | Celsius | 1.8C+32 | Fahrenheit | °F |
| ILLUMINATION | | | | |
| lx | lux | 0.0929 | foot-candles | fc |
| cd/m ² | candela/m ² | 0.2919 | foot-Lamberts | fl |
| FORCE and PRESSURE or STRESS | | | | |
| N | newtons | 0.225 | poundforce | lbf |
| kPa | kilopascals | 0.145 | poundforce per square inch | lbf/in ² |

*SI is the symbol for the International System of Units. Appropriate rounding should be made to comply with Section 4 of ASTM E380.

TECHNICAL REPORT DOCUMENTATION PAGE

| | | | |
|--|--|--|---|
| 1. Report No. | 2. Government Accession No. | 3. Recipient's Catalog No. | |
| 4. Title and Subtitle MSE WALL VOID REPAIR EFFECT ON CORROSION OF REINFORCEMENT – PHASE 2: SPECIALTY FILL MATERIALS | | 5. Report Date August, 2015 | 6. Performing Organization Code |
| 7. Author(s) E.A. Paz and A.A. Sagüés | | 8. Performing Organization Report No. | |
| 9. Performing Organization Name and Address Department of Civil and Environmental Engineering University of South Florida (USF) Tampa, FL 33620 | | 10. Work Unit No. (TR AIS) | 11. Contract or Grant No. BDV25-977-07 |
| 12. Sponsoring Agency Name and Address Florida Department of Transportation 605 Suwannee St. MS 30 Tallahassee, Florida 32399 (850)414-4615 | | 13. Type of Report and Period Covered Final Report 01/10/2014 - 08/31/2015 | 14. Sponsoring Agency Code |
| 15. Supplementary Notes | | | |
| 16 Abstract: This project provided information and recommendations for material selection for best corrosion control of reinforcement in mechanically stabilized earth (MSE) walls with void repairs. The investigation consisted of small- and large-scale experiments and modeling to examine corrosion aggravation effects and conduct durability projections. Regular cement-based controlled low-strength material (CLSM) was tested, along with slag-based CLSM, MgO-based CLSM, and polyurethane foam filler. Laboratory experiments indicated that macrocell coupling could substantially increase the corrosion of the galvanized coating in the backfill side of a void repair with CLSM based on cement or on slag. The modestly lower pH of the latter did not appear to be a sufficiently beneficial factor in lowering the extent of adverse macrocell action. CLSM based on MgO, although having a pH closer to neutral, still resulted in significant adverse macrocell corrosion development. Experiments with the polyurethane foam void fill confirmed the expectation of much lower tendency for macrocell aggravation of corrosion in the backfill side. Performance modeling projections quantified the amount of corrosion-related MSE wall degradation that may be expected as the structure ages. It is recommended that the performance model projections be analyzed via structural considerations for choice of representative limit state to establish to what extent a transition to an alternative void filler material is desirable. The use of polyurethane foam is recommended for further consideration, with additional evaluation of corrosion performance of reinforcement in that medium. | | | |
| 17. Key Words Mechanically stabilized earth walls, soil, voids, repair, CLSM, corrosion, macrocell, durability, polyurethane, galvanized, reinforcement. | | 18. Distribution Statement No Restriction This report is available to the public through the NTIS, Springfield, VA 22161 | |
| 19. Security Classif. (of this report) Unclassified | 20. Security Classif. (of this page) Unclassified | 21. No. of Pages 67 | 22. Price |

ACKNOWLEDGEMENTS

The authors acknowledge URETEK ICR., Cemex, WMC, and Premier Magnesia for assisting with the materials used for this project. The assistance of student participants in the University of South Florida, College of Engineering Research Experience for Undergraduates (David Stump, William Ruth, Leonidas Emmenegger, Juan Cardenas, Cesar Castañeda, Randy Guillen, Andrew Filippi, Thuyen Tran and Ihab Taha), is also acknowledged. The authors are indebted to Mr. Mario Paredes and Mr. Ivan Lasa from the FDOT State Materials Office for their valuable guidance.

EXECUTIVE SUMMARY

Reinforced earth walls, also called mechanically stabilized earth (MSE) walls, built with steel reinforcement are widely used in Florida. The walls typically use galvanized steel straps, strips, or rods in contact with backfill material. Placed transversely, the strips are attached to the interior surfaces of the walls, which are themselves made of reinforced concrete panels. The strips are protected from severe corrosion by requiring that the soil backfill meets FDOT specifications intended to avoid an aggressive environment.

Adverse deviation from the carefully specified initial conditions can occur as some MSE walls age, in particular because of loss of backfill resulting from excessive water ingress from the top of the wall or other settlement processes. As a result, large voids can develop that affect structural strength. Voids can be remedied by repair fill with controlled low-strength material (CLSM), also known as flowable backfill. CLSM is usually a cementitious material to be delivered as a fluid. Because of the cement content, the pore water in CLSM tends to be highly alkaline ($\text{pH} > 11$) which promotes surface passivity of embedded steel either bare or galvanized. Where present and sustained, this condition results in an extremely low corrosion rate of reinforcement on the fill side, but the overall effect may not be beneficial on the backfill side because there the reinforcement is not in the passive state. An adverse electrochemical corrosion macrocell may develop, potentially increasing greatly the rate of corrosion on the backfill side, especially near the repaired void/backfill interface. This enhanced corrosion could result in early local failure of the reinforcement due to cross-section loss.

This investigation addressed two main issues: (1) the consequences of current practices to repair these voids, by determining to what extent the macrocell (attributed to the metal buried in different media) may enhance corrosion activity of the reinforcement and (2) the control of the problem by means of alternative filling materials less prone to formation of corrosion macrocells. Materials investigated included conventional cementitious CLSM and lower pH slag- and MgO-based alternative CLSM mixtures, as well as a polyurethane foam injectable filler. The investigation consisted of both laboratory small-scale and outdoor large-scale soil corrosion test assemblies, corrosion modeling, and performance projection modeling.

The experiments indicated that macrocell coupling could substantially increase the corrosion of the galvanized coating in the backfill side of a void repair with CLSM based on cement or on slag. The modestly lower pH of the latter did not appear to be a sufficiently beneficial factor in lowering the extent of adverse macrocell action. CLSM based on MgO, although having a pH closer to neutral, still resulted in significant adverse macrocell corrosion development. Large-scale experiments showed also an indication that leach-out from the cementitious CLSM repair could induce significant macrocell action in adjacent reinforcement. Consistent with the experimental results, computer modeling also indicated that the corrosion rate of the parts of the reinforcement closest to the CLSM/backfill interface could be significantly greater (e.g., 2 times) than the average rate along the reinforcement in the backfill side, indicative of further aggravation at the interface region. Small- and large-scale experiments using a polyurethane foam void fill confirmed the expectation of much lower tendency for macrocell aggravation of corrosion in the backfill side.

Performance modeling projections quantified the amount of corrosion-related MSE wall degradation that may be expected as the structure ages. The projected deterioration for a typical design service life goal age was near nil for moderate void incidence and macrocell

corrosion aggravation near the low end of the values observed experimentally. Appreciable deterioration, to be contrasted with structurally relevant limit states, was projected for other possible regimes. It is recommended that the performance model projections be analyzed via structural considerations for choice of representative limit state to establish to what extent a transition to an alternative void filler material. If such transition is needed, the use of polyurethane foam is recommended for further consideration and evaluation. However, extended corrosion testing should be conducted to evaluate risk of corrosion at the polyurethane filler - reinforcement interface.

TABLE OF CONTENTS

| | |
|---|-------------|
| DISCLAIMER..... | ii |
| UNIVERSAL CONVERSION TABLE | iii |
| TECHNICAL REPORT DOCUMENTATION PAGE | iv |
| ACKNOWLEDGEMENTS..... | v |
| EXECUTIVE SUMMARY | vi |
| LIST OF FIGURES..... | ix |
| LIST OF TABLES..... | xii |
| LIST OF SYMBOLS | xiii |
| 1 INTRODUCTION AND OBJECTIVES | 1 |
| 1.1 Background..... | 1 |
| 1.2 Project objectives and approach..... | 2 |
| 2 TASKS PERFORMED DURING THE INVESTIGATION | 3 |
| 2.1 Selection of materials and conditions | 3 |
| 2.2 Evaluation of alternative materials..... | 5 |
| 2.2.1 Small scale experimentation..... | 5 |
| 2.2.2 Large scale experimentation..... | 18 |
| 2.2.3 Corrosion Modeling..... | 37 |
| 2.2.4 Performance projection modeling..... | 44 |
| 3 RECOMMENDATIONS..... | 50 |
| 4 CONCLUSIONS | 51 |
| 5 REFERENCES | 52 |

LIST OF FIGURES

| | |
|---|----|
| Figure 1. Diagram of small-scale specimens for testing cement-CLSM and slag-CLSM fill materials. | 6 |
| Figure 2. Diagram of soil tanks for testing of MgO-CLSM and polyurethane grout fill materials. | 7 |
| Figure 3. Specimen for in situ leaching measurements of pH. | 8 |
| Figure 4. Potential measurement of small-scale specimens. | 9 |
| Figure 5. Macrocell current measurement of small-scale specimens. | 9 |
| Figure 6. Setup of EIS measurements for small-scale specimens. | 10 |
| Figure 7. Typical EIS diagram (before surface-area normalization) obtained for galvanized steel in backfill. Specimen area was ~80 cm ² | 10 |
| Figure 8. Schematic Typical Nyquist plot showing the range and portion used to fit the surface area-normalized data. | 11 |
| Figure 9. Modified Randles equivalent circuit used to fit the data. | 11 |
| Figure 10. Potential evolution of galvanized steel electrodes (instant-off whenever applicable) buried in backfill (actual or simulated) in the different systems. | 13 |
| Figure 11. Potential evolution of galvanized steel electrodes (instant-off whenever applicable) buried in patching material in the different systems. | 14 |
| Figure 12. Apparent corrosion rate evolution of galvanized steel buried in a) backfill systems and b) CLSM systems. | 15 |
| Figure 13. Apparent corrosion rate evolution of galvanized steel buried in a) backfill systems and b) alternative filler systems. The results for polyurethane are nominal near-nil values as explained in the text. | 15 |
| Figure 14. Apparent corrosion rate evolution of non-galvanized steel in a) backfill, b) CLSM. | 16 |
| Figure 15. Macrocell current measured for the different systems. | 16 |
| Figure 16. Foundation of the soil boxes. | 19 |
| Figure 17. Assembly of the soil boxes. | 19 |
| Figure 18. Soil box assembled. | 20 |
| Figure 19. Backfill: mixture of soil with water and sodium chloride. | 20 |
| Figure 20. Dumping a batch of backfill in the soil box. | 21 |
| Figure 21. Compacting backfill in soil box. | 21 |
| Figure 22. Distribution of specimens in the first layer of the soil box. Front is the right side of the picture. | 22 |
| Figure 23. Built dam. | 22 |
| Figure 24. Backfill around the dam. | 23 |

| | |
|--|----|
| Figure 25. Second layer of specimens. | 23 |
| Figure 26. Filling of the simulated void with CLSM. | 24 |
| Figure 27. Complete removal of the dam before CLSM top-up. | 24 |
| Figure 28. Box completely filled (7/8 of the volume is backfill and 1/8 a simulated void repair with CLSM). | 25 |
| Figure 29. Filling of empty octant in box #2: a) Simulated void, b) repair using polyurethane grout, c) repaired void. | 25 |
| Figure 30. Completed box. | 26 |
| Figure 31. Box seen in perspective showing the 8 octant sections. | 27 |
| Figure 32. Distribution of reinforcement inside the boxes. | 27 |
| Figure 33. Cumulative simulated rainfall in each box. | 28 |
| Figure 34. Schematic of potential measurements. | 29 |
| Figure 35. Schematic of macrocell current measurements. | 29 |
| Figure 36. Schematic of connection for EIS tests. | 30 |
| Figure 37. Potential (instant-off whenever applicable) evolution of electrodes in box 1 (with cement-CLSM repair fill). Red lines/markers correspond to right side (side with patch); black to left. Gray dashed line corresponds to the moment of establishing the macrocell by closing the connecting switch, and blue dashed line corresponds to the start of rain simulations. | 31 |
| Figure 38. Potential (instant-off whenever applicable) evolution of electrodes in box 2 (with polyurethane repair fill). Red lines/markers correspond to right side (side with patch); black to left. Green dashed line corresponds to the moment of establishing the macrocell by closing the connecting switch when the repair material was delivered, and blue dashed line corresponds to the start of rain simulations. | 32 |
| Figure 39. Macrocell current evolution for the galvanized steel meshes in duplicate boxes 1 and 3 with cement-CLSM repair fill. Positive values indicate the mesh in the back side is anodic. Blue dashed line corresponds to the start of rain simulations. | 33 |
| Figure 40. Macrocell current evolution for the galvanized steel wire segments on back side in duplicate boxes 1 and 3 with cement-CLSM repair fill. Positive values indicate segment is anodic. Blue dashed line corresponds to the start of rain simulations. | 33 |
| Figure 41. Macrocell current evolution for the uncoated steel bars in duplicate boxes 1 and 3 with cement-CLSM repair fill. Positive values indicate the mesh in the back side is anodic. Blue dashed line corresponds to the start of rain simulations. | 34 |
| Figure 42. Macrocell current evolution for the galvanized steel meshes in duplicate boxes 2 and 4 with polyurethane repair fill. Positive values indicate the mesh in the back side is anodic. Blue dashed line corresponds to the start of rain simulations. | 34 |
| Figure 43. Macrocell current evolution for the galvanized steel wire segments on back side in duplicate boxes 2 and 4 with polyurethane repair fill. Positive values | |

indicate segment is anodic. Blue dashed line corresponds to the start of rain simulations.35

Figure 44. Macrocell current evolution for the uncoated steel bars in duplicate boxes 2 and 4 with polyurethane repair fill. Positive values indicate the mesh in the back side is anodic. Blue dashed line corresponds to the start of rain simulations.35

Figure 45. Rationale for the geometry used for model simulations.37

Figure 46. FEM domain geometry for model simulations. Rotational symmetry axis is located at the left.38

Figure 47. Ruling equations for model simulations.38

Figure 48. Corrosion potential vs. position in the reinforcement.40

Figure 49. Macrocell current density vs. position in the reinforcement.41

Figure 50. Corrosion current density vs. position (anodic portion).41

Figure 51. Model geometry for simulation with a void filled with polyurethane grout.42

Figure 52. Macrocell current distribution for the polyurethane case. Compare with Figure 49 (thin vertical feature at 3 m is interpreted as a digitization artifact).43

Figure 53. Schematic showing void distribution and effect on MSE wall reinforcement.46

Figure 54. Modeling projections showing damage function as percentage of reinforcing elements having reached their limit state at the structure age indicated. Solid line corresponds to the base case (no voids). Each family of cases corresponds to the indicated corrosion aggravation parameter k . Broken lines to the left of the base case indicate progressively greater void incidence parameters corresponding to 3%, 10%, 30%, and 100% of all elements affected by repaired voids.48

LIST OF TABLES

| | |
|---|----|
| Table 1. Mixture proportions considered for the experimental investigation | 3 |
| Table 2. Average (range) of results of pH measurements | 17 |
| Table 3. Nomenclature of the specimens | 26 |
| Table 4. Parameters used for base case modeling simulation | 39 |
| Table 5. Base case values abstracted from the BD544-32 survey [3] and assumed typical strip coating and steel thicknesses. | 47 |
| Table 6. Scenario parameters investigated | 47 |

LIST OF SYMBOLS

| | |
|------------|---|
| ACR | Apparent Corrosion Rate |
| A_i | Projected area |
| A_t | Total frontal wall area |
| ATR | Activated Titanium Rod Electrode |
| A_v | Fraction of strips affected by void presence |
| B | Coefficient used for estimating corrosion rate with Stern-Geary's Equation |
| CAP | Corrosion Aggravation Parameter (see also "k") |
| $C_g(v_g)$ | Cumulative probability distribution of v_g |
| CLSM | Controlled Low-Strength Material |
| CR_m | Corrosion rate value enhanced by macrocell coupling |
| CR_{nm} | Corrosion rate value in absence of macrocell coupling |
| $C_s(v_s)$ | Cumulative probability distribution of v_s |
| CSE | Copper - Copper Sulfate Electrode |
| D | Diffusion Coefficient |
| e | Electrons |
| E_o | Equilibrium Potential |
| Ff(t) | Damage function |
| g | Galvanized film layer thickness |
| GS | Galvanized Steel |
| i | Corrosion current density |
| i_o | Exchange current density |
| i_p | Passive current |
| k | Corrosion Aggravation Parameter value |
| MSE Wall | Mechanically Stabilized Earth Wall |
| N_i | Number of strips affected |
| n_s | Number of strips |
| P_g | Probability distribution of v_g |
| R_p | Polarization Resistance |
| s | Steel thickness |
| SCE | Saturated Calomel electrode |
| t_f | Time to reach limit state for galvanized strip |
| v | Time-invariant corrosion rate |
| v_g | Time-invariant corrosion rate of galvanized film |
| v_s | Time-invariant corrosion rate of steel |
| α | Fraction of void affected element where localized corrosion rates are greater |
| β_a | Anodic Tafel Slope |
| β_c | Cathodic Tafel Slope |
| μ | Natural logarithm of median |
| ρ | Resistivity |
| σ | Standard deviation |

1 INTRODUCTION AND OBJECTIVES

1.1 Background

Mechanically Stabilized Earth (MSE) walls are an important component in highways across the country, since their functions are many and varied (e.g., highway overpasses, bridge abutments, wing walls, etc.). The walls are designed to retain and accommodate soils in order to withstand the lateral pressure they inflict on the wall. Galvanized steel reinforcement (strips or mesh) is commonly used to stabilize the 90° slope characteristic of this type of structure by means of friction between the backfill and the reinforcement [1].

Prior research sponsored by the FDOT [2, 3] has focused on the state of MSE walls across Florida, finding that under normal circumstances (e.g., no flooding of salty water or any other contaminant), walls are generally in good shape. However, very little attention has been given to the corrosion activity of walls that have undergone a void repair. Although corrosion of galvanized steel buried in soils with different properties (such as soils with difference in compaction that lead to an aeration cell) has been researched before, little is known of the effect a cementitious repair has on the overall corrosiveness of the system.

Materials and design features are selected in order to maintain benign conditions inside the wall to minimize corrosion of the reinforcement and thereby help the wall reach a minimum service life of 75 years. To meet this goal, the backfill must meet certain criteria, such as resistivity > 3000 ohm-cm, chloride content < 100 ppm by weight of soil, sulfate content < 200 ppm, and pH value between 5 and 10 [4]. Recent surveys indicate that walls across Florida meet the designed life expectancy for these structures [2, 3]. However, there is concern regarding the effects of time and infiltration of water from sources that may include for example leaking drainage structures, and potential soil loss at damage in panel joints. Voids of significant size sometimes form behind the wall, compromising its structural integrity and durability.

Currently, the Florida Department of Transportation (FDOT) uses a cementitious material known as controlled low-strength material (CLSM) to patch these voids [5, 6]. CLSM is a mixture of cementitious materials, such as Portland cement and pozzolanic admixtures, water, and fine aggregates, formulated to be delivered as a fluid. This may be accomplished by CLSM having a smaller content of cementitious materials than regular concrete and also a larger water-to-cementitious (w/c) ratio (typically higher than one) [7].

Even though CLSM is a convenient material to patch these voids, one problem arises from the use of CLSM. The cement content, which yields pore water with high pH values ($11 < \text{pH} < 13$), creates a highly alkaline environment that promotes passivity on the surface of the reinforcing steel (bare or galvanized). The overall effect however may not be beneficial because of the electrochemical nature of corrosion and the associated interactions of a metal in contact with different backfills [8, 9, 10]. Reinforcement in simultaneous contact with backfill and CLSM initiates a macrocell corrosion process, aggravating the regular corrosion activity on the surface of the metal embedded in the backfill, which in turn behaves as a net anode. The portion of the reinforcement embedded in CLSM becomes passivated and acts as a cathode. While the anodic reaction happens only in the non-passive portion, the cathodic reaction takes place on both passive and active surfaces. The result of the amplification of the cathodic reaction due to the larger reacting surface area is greater local section loss as compared to a case where the cathodic and anodic reactions are more uniformly distributed. If severe enough, this phenomenon could result in premature failure by cross sectional loss of the reinforcement adjacent to a void repair done with alkaline CLSM.

Given the large FDOT inventory of MSE walls and the increasing service time of those structures, it is important to optimize CLSM void repairs to avoid adverse corrosion effects stemming from associated macrocell corrosion enhancement. The extent of local macrocell enhancement depends on a variety of factors which need to be considered for appropriate control. Those factors include among others the passivating properties of the CLSM pore water, overall availability of oxygen in the MSE wall body, electric resistivity of the CLSM and surrounding backfill, dimensions and physical arrangement of the strips, concentration of chloride and sulfate ions, temperature and moisture distribution. Assessment of those factors will permit determining the extent of corrosion aggravation that is taking place and the choice of alternative materials, for example a lower pH CLSM formulation, to avoid or control adverse consequences. Related issues such as the corrosion control consequences of other void injection materials occasionally used by FDOT, for example polyurethane, merit consideration as well.

This investigation addressed two main issues: (1) the consequences of current practices to repair these voids, by determining to which extent the macrocell (attributed to the metal buried in different media) may enhance corrosion activity of the reinforcement and (2) the control of the problem by means of alternative filling materials, such as a slag based flowable fill that has a lower pH than that of regular CLSM. Initial work was conducted under FDOT project BDK84-977-17 "MSE Wall Void Repair Effect on Corrosion of Reinforcement". The present project BDV25-977-07 completed the investigation. This document is a comprehensive report of the entire investigation.

1.2 Project objectives and approach

This investigation addressed two main issues: (1) the consequences of current practices to repair voids, by determining to what extent corrosion macrocells may enhance corrosion activity of the reinforcement and (2) the control of the problem by means of alternative filling materials less prone to formation of corrosion macrocells.

The approach used to achieve that objective consisted of:

- Identification of alternative materials that will keep any macrocell action to a minimum.
- Evaluation of alternative materials by:
 - Small-scale testing of current and alternative materials to identify candidates for further examination.
 - Large-scale experimentation of identified candidate materials.
- Corrosion modeling to determine the regions of severe corrosion.
- Formulation of a corrosion damage predictive model to examine alternative conditions and effect of repair practice.

The following sections detail the execution of each of the approach items and the corresponding project outcomes.

2 TASKS PERFORMED DURING THE INVESTIGATION

2.1 Selection of materials and conditions

The selections in this task were a direct result of an extensive literature review with the candidate fill materials listed in Table 1. Mixes Nos. 1, 7, 10, 15 and 17 were initially identified in consultation with the project manager as a narrowed list for further evaluation. Of all available mixes, No. 7 was selected for preliminary small-scale experimentation as it is typical of materials used for this type of applications in current practice and larger scale applications. Mix 15 was retained as a possible alternative, since a slag-only CLSM fill was suggested by the Project Manager for additional evaluations.

Results of that initial testing with Mix 7 indicated that fully saturated conditions (replicating earlier work by Trejo et al. [8 - 10]) were not the best representation of the interior of a typical MSE Wall because of insufficient oxygen access. In follow up experiments an improved backfill simulation was conducted consisting of a mix of crushed limestone and sand (instead of sand only as used in the preliminary experiment) to better represent the backfill in an actual MSE Wall. A mild level of chloride contamination (100 ppm of soil mass) was used.

Additionally, given that results obtained in the previous phase for slag-CLSM systems showed no significant difference from those of cement-CLSM, since the pH of slag-CLSM (results of which are shown in the following section) was not all that different from that of regular cement-CLSM, more alternative materials were needed in order to narrow down the list of candidates. Magnesia-based cements (mix 16) typically yield pore water with a pH value close to neutrality [11], making it an ideal material to test for this project. Furthermore, polyurethane grout (mix 17) has been gaining widespread use for repairing voids found in MSE walls [12], thus assessing its corrosive nature could also yield another possible choice to test at the large-scale.

Table 1. Mixture proportions considered for the experimental investigation

| # of mix | cement Content (lb/cy) | Fly ash content (lb/cy) | slag (lb/cy) | Fine Aggregate (lb/cy) | Water (lb/cy) | Air Entrainer (oz) | Retardant (oz) | Source |
|----------|------------------------|-------------------------|--------------|------------------------|---------------|--------------------|----------------|--|
| 1 | 102 | 304 | 0 | * | 348 | 0 | 0 | Trejo et al. 2005 [8] |
| 2 | 51 | 607 | 0 | * | 531 | 0 | 0 | Trejo et al. 2005 [8] |
| 3 | 102 | 0 | 0 | * | 230 | 0 | 0 | Trejo et al. 2005 [8] |
| 4 | 60 | 290 | 0 | * | 458 | 2 | 0 | Pons et al. 1998 [13] |
| 5 | 75 | 0 | 150 | 2720 | 408 | 10 | 0 | FDOT State Project No. 872 Final Report [14] |

Table 1. Continuation. Mixture proportions considered for the experimental investigation

| # of mix | cement Content (lb/cy) | Fly ash content (lb/cy) | slag (lb/cy) | Fine Aggregate (lb/cy) | Water (lb/cy) | Air Entrainer (oz) | Retardant (oz) | Source |
|--|---|-------------------------|--------------|------------------------|---------------|--------------------|----------------|--|
| 6 | 150 | 0 | 595 | 2170 | 408.2 | 12 | 50 | FDOT State Project No. 872 Final Report [14] |
| 7 | 100 | 0 | 0 | 2163 | 391.5 | 3 | 0 | FDOT State Project No. 872 Final Report [14] |
| 8 | 125 | 0 | 152 | 2055 | 391.5 | 3 | 0 | FDOT State Project No. 872 Final Report [14] |
| 9 | 90 | 0 | 0 | 2398 | 458 | 15 | 0 | FDOT State Project No. 872 Final Report [14] |
| 10 | 150 | 0 | 250 | 2475 | 500 | 5 | 0 | FDOT State Project No. 872 Final Report [14] |
| 11 | 79 | 0 | 0 | 2385 | 500 | 4.1 | 3.2 | FDOT State Project No. 872 Final Report [14] |
| 12 | 150 | 595 | 0 | 2103 | 484 | 4.5 | 6 | FDOT State Project No. 872 Final Report [14] |
| 13 | 50 | 250 | 0 | 2860 | 370 | 3.5 | 0 | FDOT State Project No. 872 Final Report [14] |
| 14 | 50 | 0 | 0 | 2475 | 25 gal/cy | 3 | 0 | City of Cleveland Specifications [15] |
| 15 | 0 (slag only mix) | 0 | 757 | 2533 | 757 | 0 | 0 | Tasha et al. 2007 [16] |
| 16 | 100 ^ | 0 | 0 | 1500 | 500 | 0 | 0 | Iyengar and. Al-Tabbaa. 2007 [11] |
| 17 | Polyurethane Filling. (e.g., PRIME FLEX 985 or a Polyurethane fill currently used by FDOT in any of their fields of operation). | | | | | | | |
| * Add necessary amount to yield 1 cy of CLSM ^ Magnesia cement based CLSM mix | | | | | | | | |

2.2 Evaluation of alternative materials

2.2.1 Small-scale experimentation

Methodology:

Experimental set up

In order to test cement-CLSM and slag-CLSM, cylindrical specimens (Figure 1) were prepared using mixes #7 (based on cement) and #15 (based on slag) in Table 1. The embedded electrodes were 1 ft.-long, ½ in diameter wires cut out of a sample of galvanized soil reinforcement mesh provided by FDOT. Area of each specimen in direct contact with the cell medium was ~ 80 cm². All cells contained a centrally placed Activated Titanium Rod (ATR) reference electrode. An activated Titanium wire mesh counter electrode (C.E.) was placed on the inner perimeter of the cell. The test cells were based on 4 x 8 in concrete cylinder molds. One half of the cell was filled with CLSM placing the cylinder horizontally with a baffle at the end, and allowing it to set for 3 days. Afterwards the baffle was removed, cells were placed vertically and the other half was filled backfill. The backfill consisted either of simulated backfill (prepared using a mixture of 70% crushed limestone + 30% silica sand), or actual backfill with resistivity ~ 3000 ohm-cm. The latter consisted of material meeting AASHTO Type A-3 [17] backfill (fine sand with less than 10% passing 200 sieve, as per FDOT specifications) supplied by Angelo's Recycled Materials, St. Petersburg, Florida. This material was also used for the large soil boxes described in the Large-scale Experimentation section 2.

Physical properties of the backfills included: a porosity close to 40% (meaning about 40% of the backfill volume is void space). Water was added to the backfills to obtain a level of moisture of 45% (corresponding to 45% of the void space filled with water). The water for the laboratory specimens was distilled water to which NaCl was added to create a mild chloride contamination of 100 ppm (a worst-case scenario corresponding to the upper limit of the chloride threshold set by FDOT guidelines for MSE wall backfill [4]).

In some of the cells the wires embedded in the backfill and in the CLSM sides were left disconnected from each other, to evaluate the corresponding self-corrosion in that uncoupled condition. In other cells containing both backfill and filler, the wires were permanently interconnected to evaluate the macrocell corrosion flowing between them in that coupled condition. All cells had a sealing lid to minimize water evaporation.

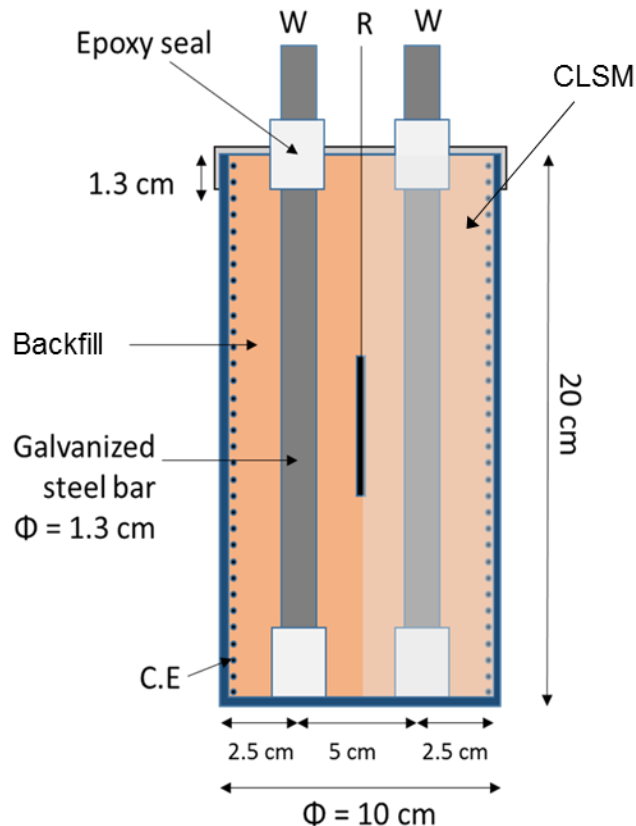


Figure 1. Diagram of small-scale specimens for testing cement-CLSM and slag-CLSM fill materials.

In order to test additional candidate materials such as MgO-based CLSM and polyurethane grout, small-scale experiments were also conducted with 15 x 15 x 22 inch soil tanks to better represent geometry of MSE walls. Additionally, larger-sized cells provided the opportunity to include more testing electrodes (8 in total) compared to only 2 in cylinders. The new cell were half filled with actual backfill and half with magnesia-based CLSM (Figure 2), which has a lower pore water pH than slag and cement based CLSM mixes. Each half contained a reinforcing mesh segment, a galvanized steel wire and two plain steel wires. The area of contact with the medium of each bare steel specimen was ~ 80 cm², for OC galvanized steel ~ 50 cm² and for galvanized steel mesh segments ~ 170 cm². Additionally, all soil tanks contained an ATR reference electrode on each half of the cell. The reinforcing mesh segment of each half were connected to each other, as were two of the plain steel specimens to establish the macrocell. Similarly, preliminary macrocell experiments were conducted with the same configuration using commercially available expansive polyurethane foam (GREAT STUFF™ Big Gap Filler) to determine the macrocell corrosion response of the system. The specimens evaluated for macrocell enhancement were normally interconnected and the macrocell current flowing between them was periodically measured. The electrodes placed in the polyurethane side were conditioned beforehand by burying them in moist Type A-3-select for use as backfill in MSE walls for a period of 2 weeks. That treatment allowed for some prior corrosion to take place, thus causing a preexisting thin layer of corrosion product/backfill attached to the surface of the electrodes. That layer simulated the expected condition of reinforcement that has been exposed in an MSE wall for some time before a void developed. The preexisting porous and moist layer allows for some degree of electrolytic contact between the surface of the

polyurethane-embedded reinforcement and the rest of the soil in the system, with associated possible corrosion development. This situation was similarly considered for the modeling calculations presented in Section 2.2.3. For the laboratory tests the preconditioning was important, as otherwise embedment of pristine reinforcement in essentially insulating polymeric foam would have had little chance to reveal potential corrosion risk in an actual field application.

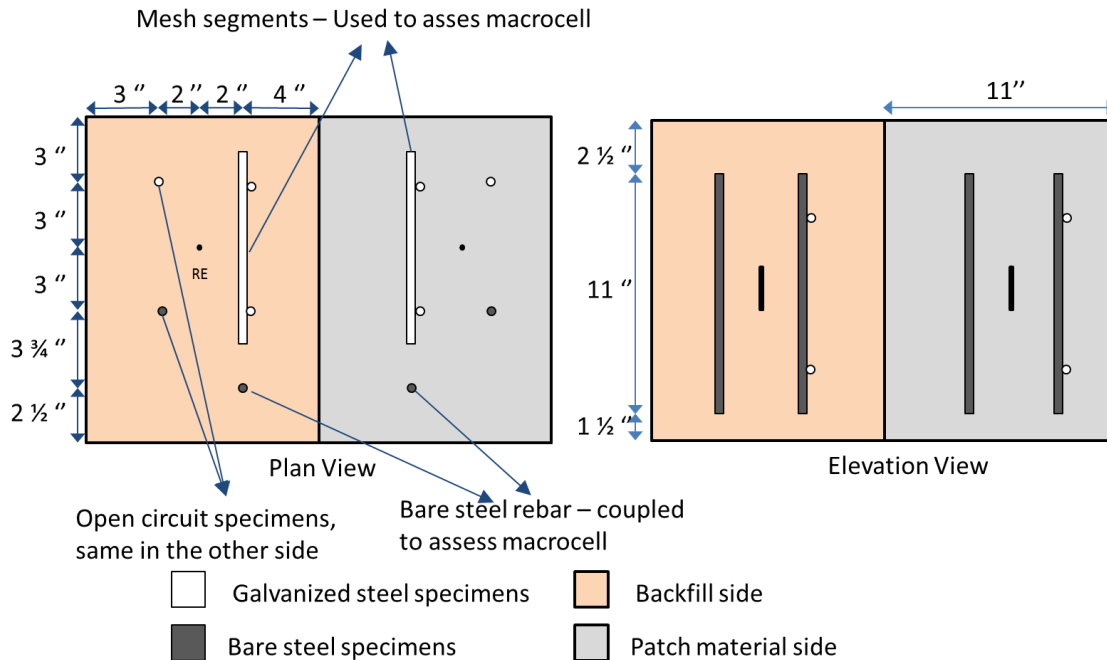


Figure 2. Diagram of soil tanks for testing of MgO-CLSM and polyurethane grout fill materials.

CLSM specimens were also cast in 3 x 6 in (7.5 x 15 cm) plastic mold cylinders (Figure 3) in order to conduct pH measurements of the pore water by the in-situ leaching technique [18,19,20]. Two cylinders were cast for each CLSM mix. Three holes 1/8 in (0.3 cm) in diameter were drilled to a depth of 1-3/16 in (3 cm) into each specimen, after which ~0.25 mL of deionized and decarbonated water was added to each hole. Some of the water was absorbed so the water was replenished almost daily for the first week and then weekly from then on. After equilibrium was reached about 3 weeks in, in-situ measurements as described elsewhere [18,20] were performed using an activated titanium wire as a pH sensing electrode and a silver – silver chloride microelectrode as a reference electrode. Measurements were performed periodically to allow for stabilization of the cementation reactions. The values reported here are for the end of a 90-day stabilization period. The pH of the backfill was measured separately using the Florida method of test for pH of soil and water [21]; given the non-reacting nature of the soil a stabilization period of only 1 day was used.

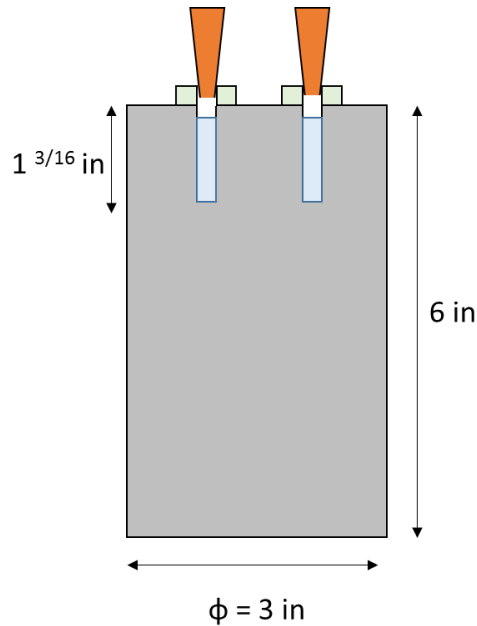


Figure 3. Specimen for in situ leaching measurements of pH.

Measurements and monitoring:

Potentials were measured with a 200 M-ohm input impedance MCM multimeter model LC-4.5. The red (positive) connection was connected to the working electrode, whereas the black (negative) connection was connected to the ATR reference electrode (Figure 4). Calibration of the ATR reference electrode was performed periodically with a Saturated Calomel Electrode (SCE); potential measurements are reported in the SCE scale. Macrocell current measurements were periodically taken to monitor corrosion enhancement using an HP multimeter model 34401A (0.1-ohm input resistance, configured as an ammeter) by connecting the red (positive) connection to the suspected anode and the black (negative) to the suspected cathode (Figure 5). The regular connection between both electrodes was then temporarily interrupted allowing the current to flow through the ammeter. The current was measured also after switching the ammeter cables (red connected to cathode and black to anode), and the results of both measurements were averaged with appropriate sign to obtain a value where and instrumental bias was canceled out. Corrosion rate measurements of small-scale uncoupled specimens were also performed by means of Electrochemical Impedance Spectroscopy (EIS) with a Gamry Reference600 Potentiostat/Galvanostat/ZRA using a frequency sweep from 100 kHz to 1 mHz and recording 5 points/decade (Figure 6). The color-coded green and blue terminal cables were connected to the working electrode, the white terminal cable to the reference electrode and the red terminal cable to complete the circuit was connected to the counter electrode.

Data Processing:

Typical EIS spectra (Figure 7) presented significant high frequency dispersion in the form of an apparent constant imaginary component. Hence only the lowest frequency decade (5 data points ranging from 1 mHz to <10 mHz) were used for analysis (Figure 8) to obtain an estimate of the surface-area normalized Polarization Resistance (R_p), by fitting to a modified Randles equivalent circuit (Figure 9) that included a Constant Phase angle Element (CPE) and a nominal solution resistance (R_s) [22]. This is a provisional evaluation method that is a subject of a continuing investigation [23].

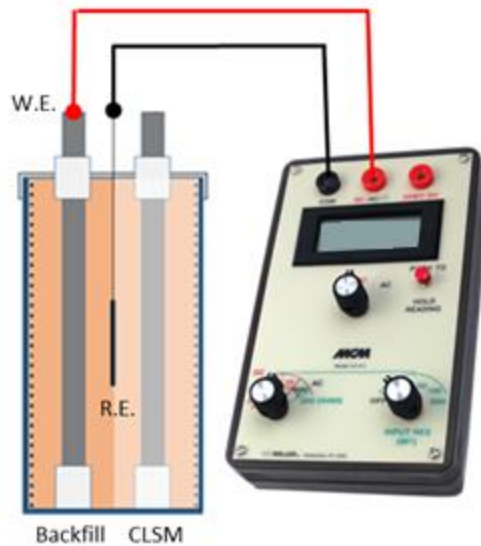


Figure 4. Potential measurement of small-scale specimens.

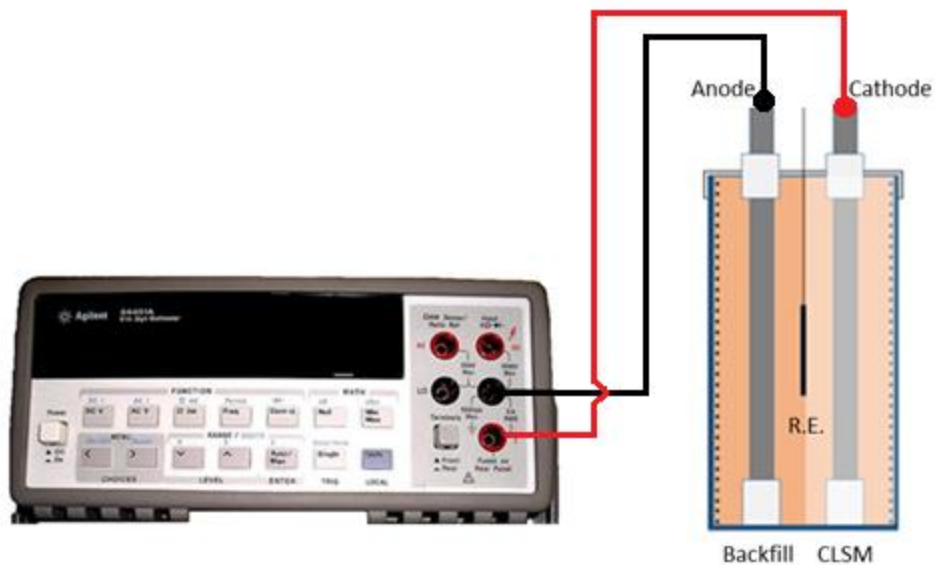


Figure 5. Macrocell current measurement of small-scale specimens.

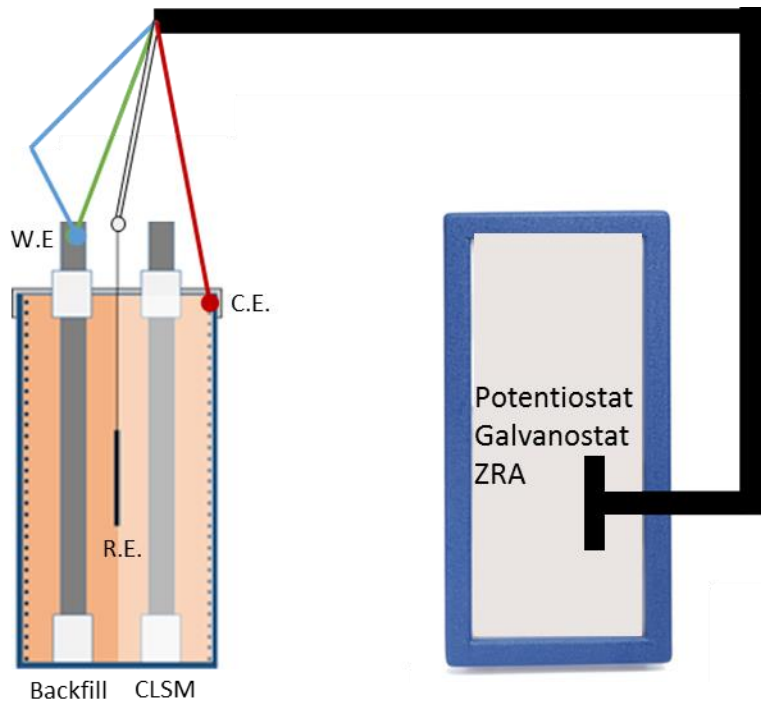


Figure 6. Setup of EIS measurements for small-scale specimens.

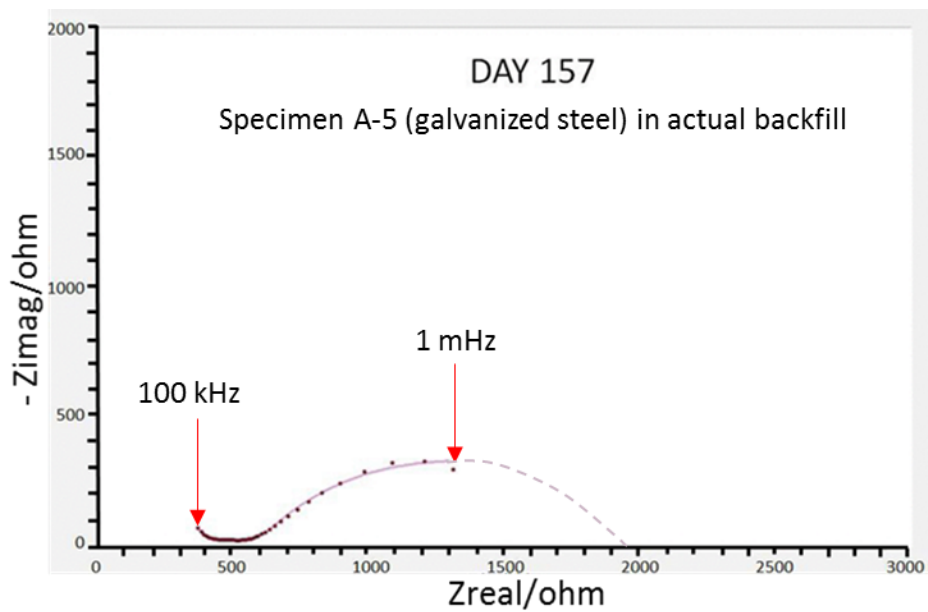


Figure 7. Typical EIS diagram (before surface-area normalization) obtained for galvanized steel in backfill. Specimen area was $\sim 80 \text{ cm}^2$.

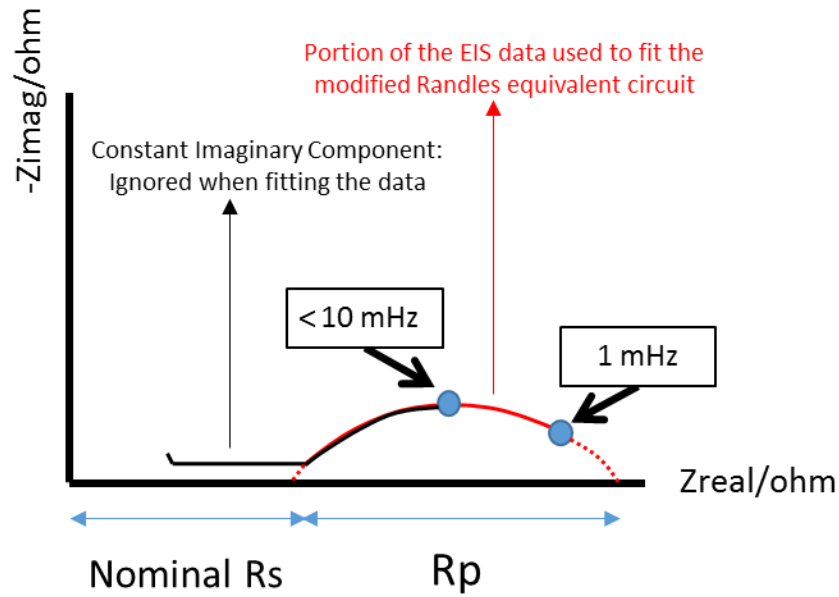


Figure 8. Schematic Typical Nyquist plot showing the range and portion used to fit the surface area-normalized data.

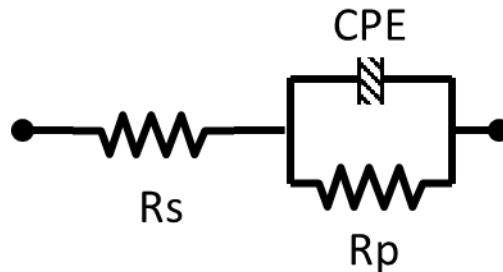


Figure 9. Modified Randles equivalent circuit used to fit the data.

Once R_p was obtained, and by means of the Stern-Geary equation [24,26] the apparent corrosion current density was obtained:

$$i = \frac{B}{R_p} \quad \text{Eq. 1}$$

for zinc $B \sim 0.022 \text{ V}$ [25].

An estimation of the corrosion rate as metal loss per unit of time was obtained using the Faradaic conversion for zinc whereby $1 \mu\text{A}/\text{cm}^2$ corresponds to approximately $15 \mu\text{m}/\text{y}$ [25]. The result is designated as the Apparent Corrosion Rate (ACR).

Results:

In here and in the following, results from duplicate or multiple replicate specimens are presented either as a group or as average results for a group with scatter bands indicating the range of values. In some figures, the scatter bands disappear after ~420 days because one of the duplicate specimens was extracted for subsequent visual examination of the wire.

Figure 10 shows the potential evolution of uncoupled wires in simulated and in actual backfill, showing similar trends toward stabilization to values ≤ -0.5 V, suggestive of an actively corroding condition⁽¹⁾. Figure 11 shows the potential evolution in all types of fillers. Specimens in cementitious-based fillers share a general trend of stabilizing towards a more noble potential (> -0.6 V), especially for the slag CLSM (~ 0 V), indicative of generally passive behavior. For specimens embedded in polyurethane foam potential readings were poorly defined and near 0 V. This situation is thought to indicate that despite the preconditioning procedure, electrolytic contact between the specimen and the reference electrode was insufficient to obtain a reliable potential measurement.

Overall, for cementitious filler instances the trends are generally consistent as expected with the establishment of a macrocell, where potentials of galvanized steel in the backfill side are more negative (anode) than of those on the filler side (cathode).

Figure 12 and Figure 13 shows the ACR of the uncoupled wires, obtained from the EIS tests. For the cementitious fillers, results indicated that in the absence of a macrocell connection, the ACR of wires buried in either simulated or actual backfill was nearly the same, and consistently several times greater than that of wires in cement, slag or MgO CLSM. For the CLSMs, (as shown in Figure 13b) there was a trend toward long-term ACR values approaching $0.1 \mu\text{m}/\text{y}$, as would be expected for a passive regime. Thus, the ACR results of the disconnected elements were consistent with the indications of the open circuit potential results. Corrosion rates of bare steel in regular soil and CLSM followed a similar trend as the galvanized steel specimens (Figure 14).

ACRs for galvanized steel in polyurethane foam were determined on a nominal basis considering that potential measurements were generally unreliable as noted above. Nyquist diagrams suggested very high R_p values, which yielded on analysis extremely low ACR values, in the order of $1 \times 10^{-5} \mu\text{m}/\text{y}$ throughout the monitoring period.

⁽¹⁾ Based on the results shown in Figures 10 and 11, the behavior of the reinforcement in actual or simulated backfill was deemed to be equivalent, so for interpretation of results, both types of backfill were considered as interchangeable.

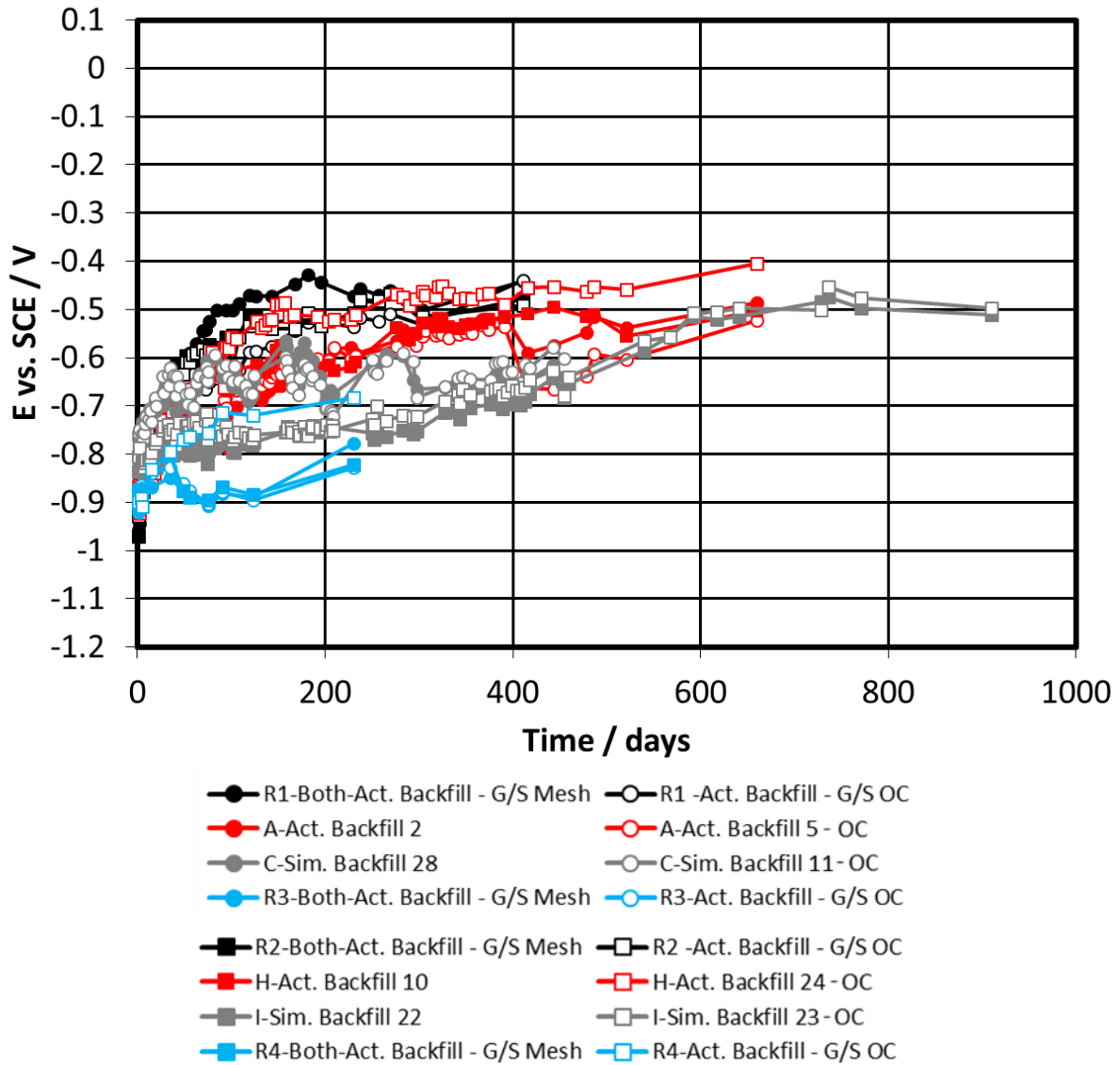


Figure 10. Potential evolution of galvanized steel electrodes (instant-off whenever applicable) buried in backfill (actual or simulated) in the different systems.

Marker Code:

Black: GS in actual backfill for the MgO-CLSM/Actual backfill system.

Red: GS in actual backfill for the slag-CLSM/Actual backfill system.

Grey: GS in simulated backfill for the cement-CLSM/simulated backfill system.

Blue: GS in actual backfill for the Polyurethane/actual backfill system.

OC: open circuit specimens, all others instant-off values in coupled systems.

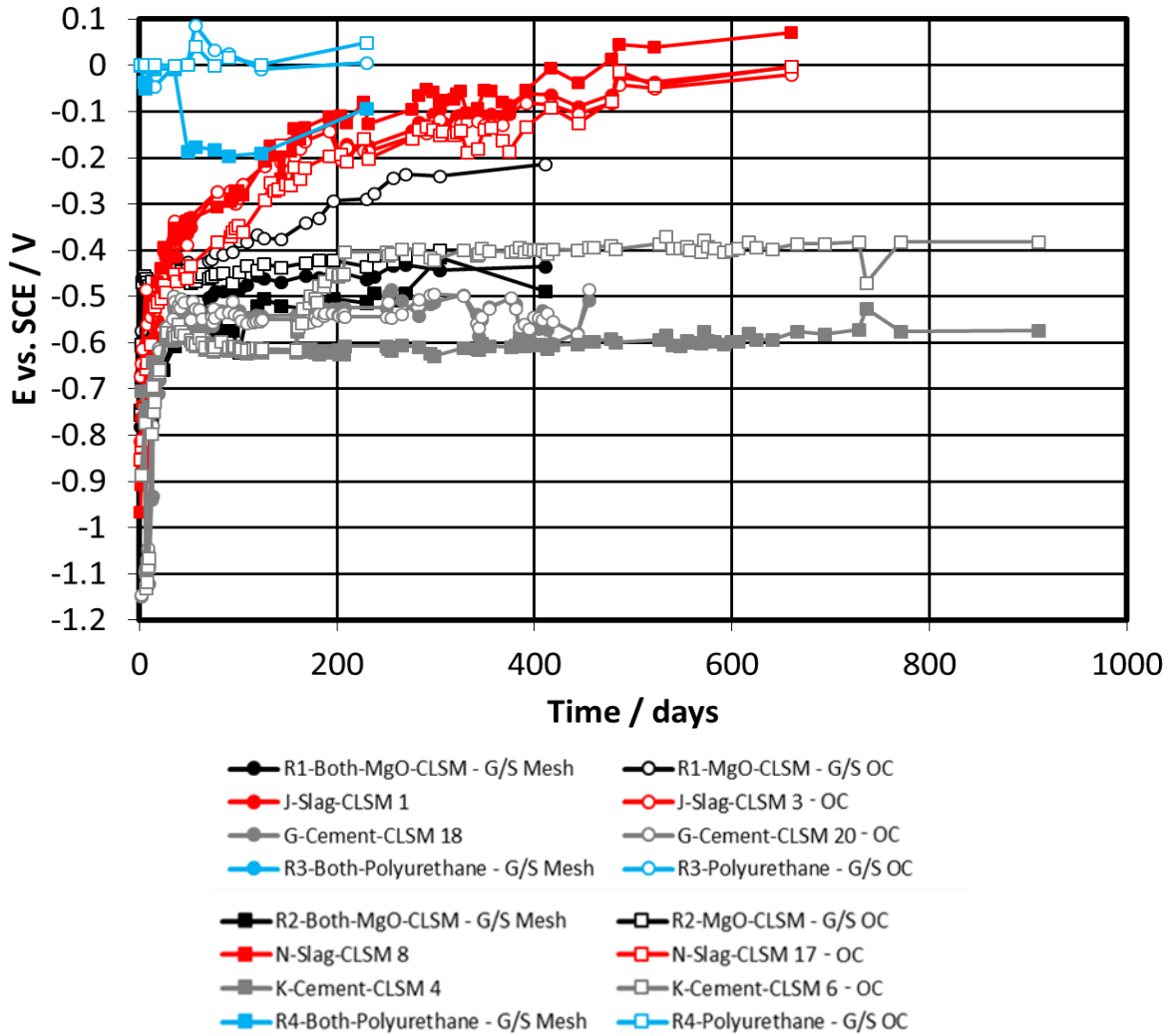


Figure 11. Potential evolution of galvanized steel electrodes (instant-off whenever applicable) buried in patching material in the different systems.

Marker Code:

Black: GS in MgO-CLSM the MgO-CLSM/Actual backfill system.

Red: GS in slag-CLSM for the slag-CLSM/Actual backfill system.

Grey: GS in cement-CLSM for the cement-CLSM/simulated backfill system.

Blue: GS in Polyurethane for the Polyurethane/actual backfill system.

OC: open circuit specimens, all others instant-off values in coupled systems.

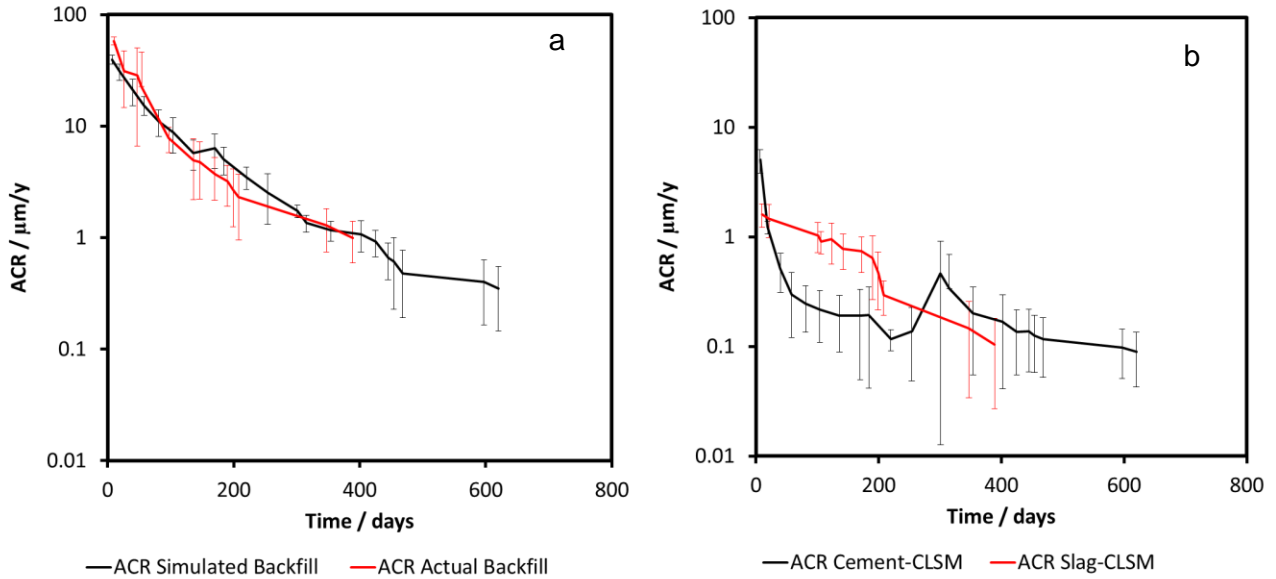


Figure 12. Apparent corrosion rate evolution of galvanized steel buried in a) backfill systems and b) CLSM systems.

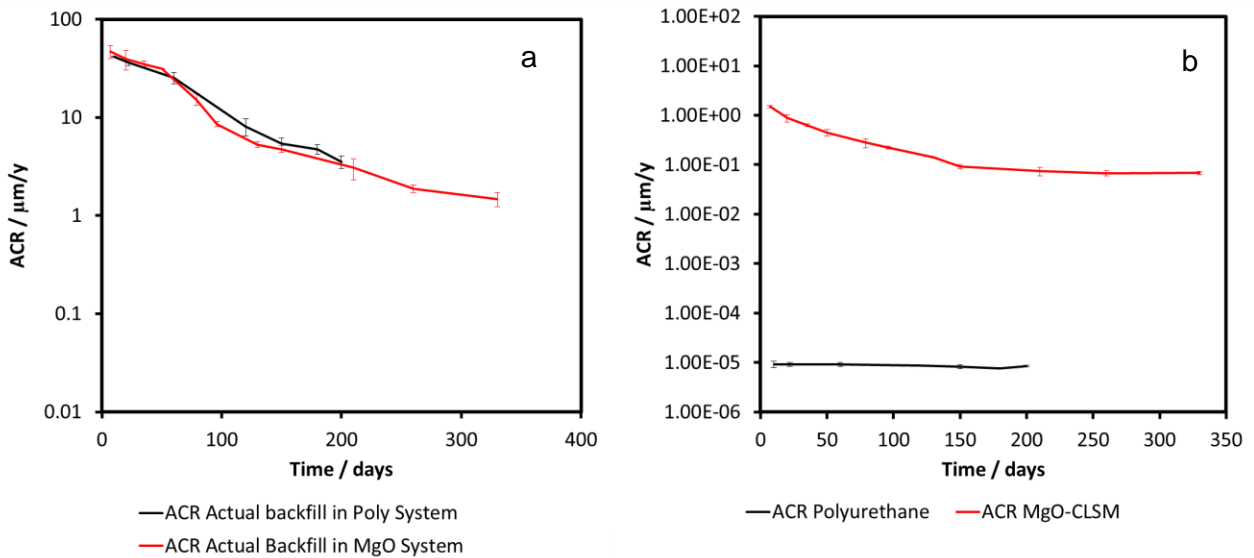


Figure 13. Apparent corrosion rate evolution of galvanized steel buried in a) backfill systems and b) alternative filler systems. The results for polyurethane are nominal near-nil values as explained in the text.

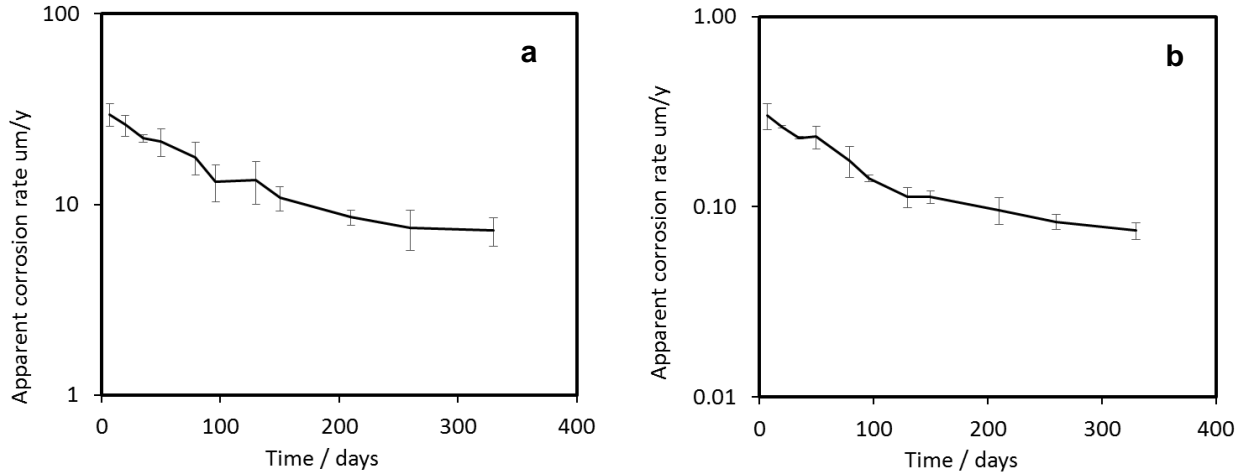


Figure 14. Apparent corrosion rate evolution of non-galvanized steel in a) backfill, b) CLSM.

The macrocell current results for all the systems evaluated are shown in Figure 15, after converting into current densities by dividing the macrocell current measured by the area of the anodic wire. For the CLSM systems the macrocell anode was always found to be, as expected, on the backfill side of the cell.

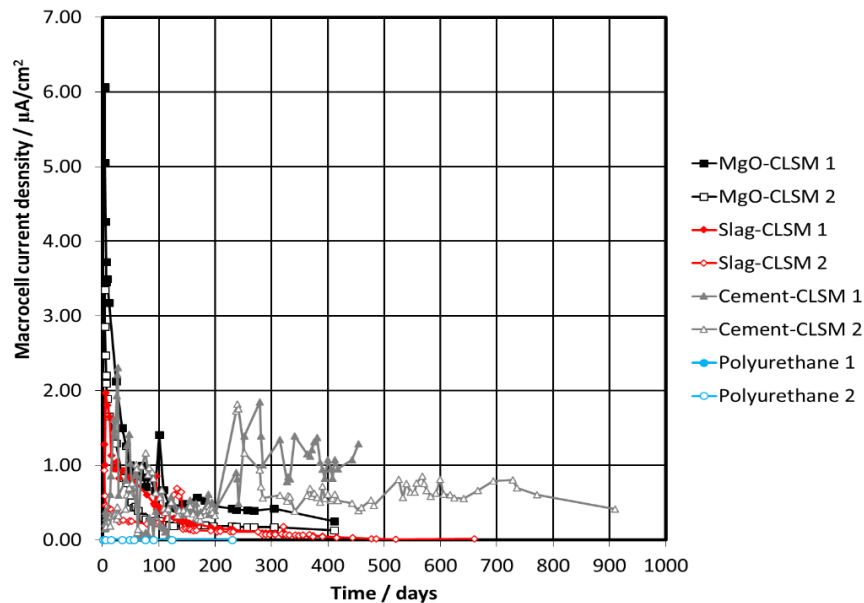


Figure 15. Macrocell current measured for the different systems.

Marker Code:

Black: GS in the MgO-CLSM/Actual backfill system.

Red: GS in the slag-CLSM/Actual backfill system.

Grey: GS in the cement-CLSM/simulated backfill system.

Blue: GS in the Polyurethane/actual backfill system.

The result, after Faradaic conversion was treated as an extra metal loss on the anode side. Considering the ACR metal loss estimates obtained separately for the disconnected specimens as self-corrosion, a nominal total metal loss was estimated by adding the extra and self-components

The instantaneous total metal loss was integrated over the first 420-day exposure period and converted into an equivalent total metal loss on the anodic wire. Self-corrosion data for the same period indicated average self-corrosion amounts of ~8 μm for the wires in both actual and simulated backfill. Combining results of extra and self-components yielded estimated average total combined loss of galvanized film thickness of 12 μm, 20 μm and 17 μm when coupling to reinforcement in the slag-, cement- and MgO-CLSM media respectively. These values are about twice those estimated for self-corrosion loss, indicating that in those three CLSM cases macrocell coupling aggravated average corrosion on the anode to that extent during that period. This corrosion enhancement will be hereon expressed in the form of a Corrosion Aggravation Parameter (CAP) defined as:

$$k = CR_m / CR_{nm} \quad \text{Eq. 2}$$

where CR_m is the corrosion rate value where it has been enhanced by macrocell coupling, and CR_{nm} is the corrosion rate that would have taken place in the absence of macrocell coupling. Hence in the above examples $k \sim 2$. This parameter, evaluated from the data presented here and in Section 2.2.2 is a key input in the model proposed in Section 2.2.4, Performance Projection Modeling.

Table 2 presents the pH results. Both backfill media are close to neutrality, complying with FDOT specifications [1]. In contrast the slag and cement CLSM are distinctly alkaline, capable of promoting passivation of the galvanized surface[26], whereas MgO-CLSM's pH was much closer to neutrality, as expected.

Table 2. Average (range) of results of pH measurements

| | | |
|-----------------|------------|--------------|
| Backfill | Simulated | 7.78 (0.13) |
| | Actual | 6.04 (0.08) |
| CLSM | cement | 12.42 (0.04) |
| | slag | 11.51 (0.12) |
| | MgO-cement | 7.64 (0.31) |

For the urethane cells the macrocell current was nearly nil, without a clear anode or cathode designation for either side of the cell. By analogy with the treatment used for the CLSM tests, the equivalent value of the CAP for the polyurethane cases is equal to 1, indicating no corrosion aggravation from macrocell sources for the user of this filler material.

2.2.2 Large-scale experimentation

Methodology

Experimental Setup

Four large scale soil boxes were built. Boxes 1 and 3 had a simulated void filled with cement CLSM, whereas boxes 2 and 4 had the simulated void filled with polyurethane grout.

The large scale soil boxes (approximately 8 ft long x 4 ft wide x 3 ft high) were assembled by building a wooden frame for each individual wall of the box and then nailing $\frac{3}{4}$ in thick plywood to the respective frame. Finally, all four walls were put together on site (Figure 16 through Figure 22). The boxes were filled by making 50-kg batches of the backfill and dumping it in the boxes each time. Approximately 3.4 tons of backfill were added to fill $\frac{7}{8}$ of the box. The remaining $\frac{1}{8}$ was filled with approximately 500 kg of patching material (mix 7 in Table 1). Every fourth batch of backfill was compacted by means of a tamper until enough backfill was dumped to reach 8 in of backfill. The specimens were then placed in the box, connecting wires placed, and an additional layer of 8 in was placed on top of the electrodes, following the same methodology. After the second layer of backfill was placed, the simulated void, which occupies $\frac{1}{8}$ of the box space, had to be enclosed using a specially built dam that allows for the continuous galvanized steel rebar to go from end to end. After the dam was in place, filling of the box continued around it. For boxes 1 and 3 the dam was then slowly taken out of the box as the patching material filled the simulated void (Figure 23 through Figure 28).

For polyurethane void filling in the large-scale boxes 2 and 4, the dam, which prevented the sides of the simulated void from collapsing was removed (Figure 29, a) just before filling. The electrode array for the octant to be polyurethane filled was previously conditioned with moist backfill to better represent field conditions as discussed earlier in Section 2.2.1. This preconditioning (other than natural exposure to moist air for several months prior to CLSM filling) was not deemed necessary for the CLSM boxes, since electrolyte access after filling was abundant there. Once the simulated void was completely exposed, a 2 component system (486STAR, provided by URETEK ICR.) polyurethane grout was pumped using a special pump that delivered both components on a 1:1 ratio by the personnel from URETEK ICR., who actually performed the patching (Figure 29, b) by filling the empty octant with the polyurethane grout until it was level with the backfill upper surface (Figure 29, c).

After the fill was put in place and allowed to set, a more permanent cover made of wood was placed on top of all boxes (Figure 30) to protect them from the environment. An initial battery of measurements was performed, and 2 days afterwards, the macrocell was established, and monitoring of the newly patched boxes continued.



Figure 16. Foundation of the soil boxes.



Figure 17. Assembly of the soil boxes.



Figure 18. Soil box assembled.



Figure 19. Backfill: mixture of soil with water and sodium chloride.



Figure 20. Dumping a batch of backfill in the soil box.



Figure 21. Compacting backfill in soil box.



Figure 22. Distribution of specimens in the first layer of the soil box. Front is the right side of the picture.



Figure 23. Built dam.



Figure 24. Backfill around the dam.



Figure 25. Second layer of specimens.



Figure 26. Filling of the simulated void with CLSM.



Figure 27. Complete removal of the dam before CLSM top-up.



Figure 28. Box completely filled (7/8 of the volume is backfill and 1/8 a simulated void repair with CLSM).



Figure 29. Filling of empty octant in box #2: a) Simulated void, b) repair using polyurethane grout, c) repaired void.



Figure 30. Completed box.

The boxes' interior consists of 4 front-to-back quadrants, each including a front and a back octant. Each octant of the box contained one large (~ 2 ft x 3 ft) galvanized steel mesh specimen, one sandblasted uncoated steel rebar simulating material where the galvanized layer had been consumed, and small galvanized bar segments near the transition with the nearest octant. Moreover, each quadrant contained one galvanized continuous bar spanning two octants in the long direction of the box. Specimen nomenclature is given in Table 3. Figure 31 shows the distribution of the octants in 3-D perspective, while Figure 32 details the distribution of specimens within the box. Wiring with normally connecting interrupting switches were placed between the front and back electrodes of each kind (e.g., mesh-to-mesh) in each quadrant. The galvanized bar segments within each octant were also normally connected via an interrupting switch to the galvanized mesh in the same segment, allowing for measurement of the individual current to the segment.

Table 3. Nomenclature of the specimens

| Position | | | Type of specimen |
|-----------|-----------|----------|-------------------------------|
| Left (L) | Front (F) | Up (U) | Mesh (M) |
| | | Down (D) | Uncoated steel (S) |
| | Back (B) | Up (U) | Galvanized continuous bar (C) |
| | | Down (D) | Galvanized bar segments (G) |
| Right (R) | Front (F) | Up (U) | |
| | | Down (D) | |
| | Back (B) | Up (U) | |
| | | Down (D) | |

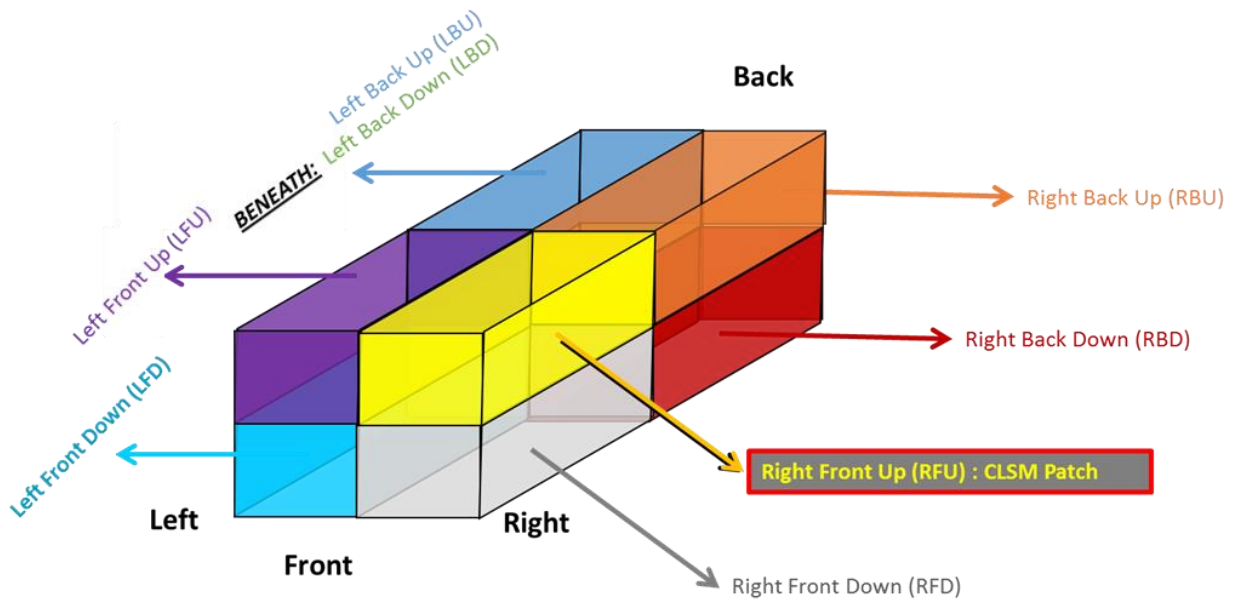


Figure 31. Box seen in perspective showing the 8 octant sections.

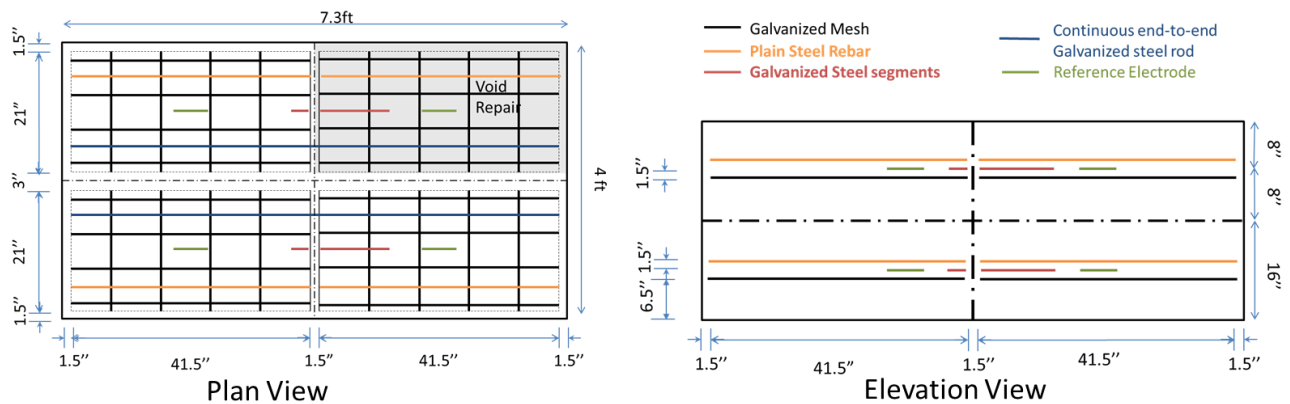


Figure 32. Distribution of reinforcement inside the boxes.

Additionally, rain simulation was carried out as well to determine the effect of water intrusion during possible rainstorms. In the state of Florida, approximately 60 inches of rainfall are expected in a yearly basis [27]. Taking into consideration dimensions of the boxes and an approximate daily rate of 0.16 inches of water, each box was scheduled to receive the equivalent of a volume of approximately 11.8 kg of water per day.

To simulate rainfall, rain water was actually collected from roof runoff or simulated by filtering tap water from the University of South Florida (USF) system to lower hardness and have an overall resistivity greater than 3000 ohm-cm. Water was applied periodically at the target rate by spraying on the soil surface of the box while temporarily removing the cover.

Simulated rainfall accumulation in cm is shown in Figure 33, where the blue dashed line represents an ideal cumulative rainfall. Up to approximately day 150, approximately 63 cm of rain have been sprayed to each box. Initially simulated rain was applied daily and about weekly afterwards.

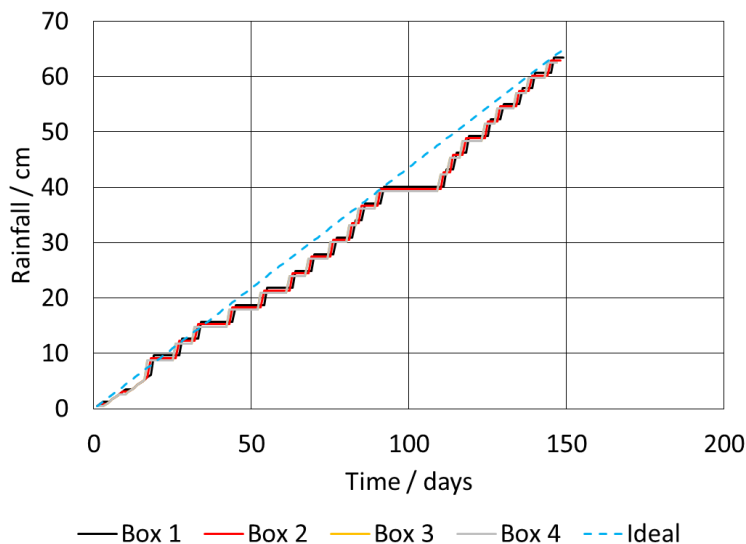


Figure 33. Cumulative simulated rainfall in each box.

Measurements and monitoring:

Current and potential measurement methodology was analogous to that used for the small-scale experiments. All measurements were taken through the connection terminals located in the control panel, but for simplicity the following Figures show direct connections.

Potentials were measured using the same type of voltmeter and similar methodology of assigning polarity. Here, however, since all working electrodes were coupled to the matching element on the other end of the box (e.g., front mesh connected to back mesh), both sides of the macrocell were momentarily uncoupled to measure the instant off potential and then coupled back again immediately (Figure 34). Also, macrocell currents were measured following the same methodology and equipment as in the small-scale experiments (Figure 35). The ATR electrodes were periodically calibrated against external Cu-CuSO₄ electrodes (CSE) while temporarily opening all electrode-interconnecting switches; all potential results for the large-scale boxes are given in the CSE scale.

EIS measurements for the large-scale experiments were carried using a Gamry potentiostat/galvanostat/ZRA. Measurements were conducted independently for each component of a macrocell. To that end the portion of the macrocell to be tested was under Alternating Current (AC), uncoupled from the rest, while keeping the Direct Current (DC) polarization at the normally connected level. This was achieved by a high impedance current source was previously calibrated to deliver the same amount of Direct Current (DC).

Interelectrode current measured before impedance measurements were carried out. The positive terminal of the source removes electrons from the anode and thus is connected to it, while the negative terminal delivers the electrons to the cathode. Once the current source was adjusted and working, the terminals were connected as shown in Figure 36.

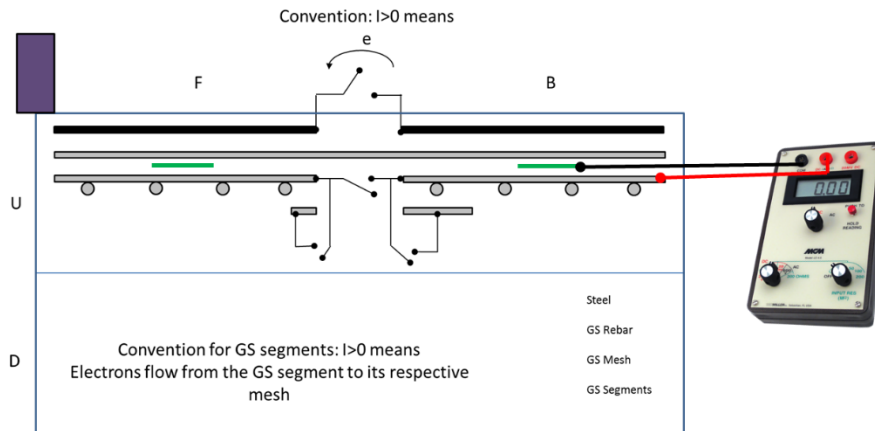


Figure 34. Schematic of potential measurements.

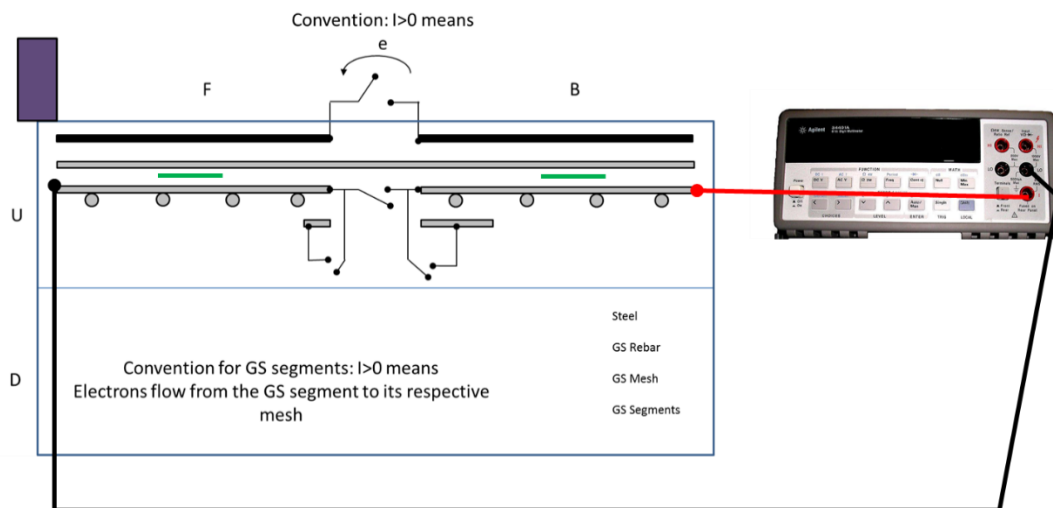


Figure 35. Schematic of macrocell current measurements.

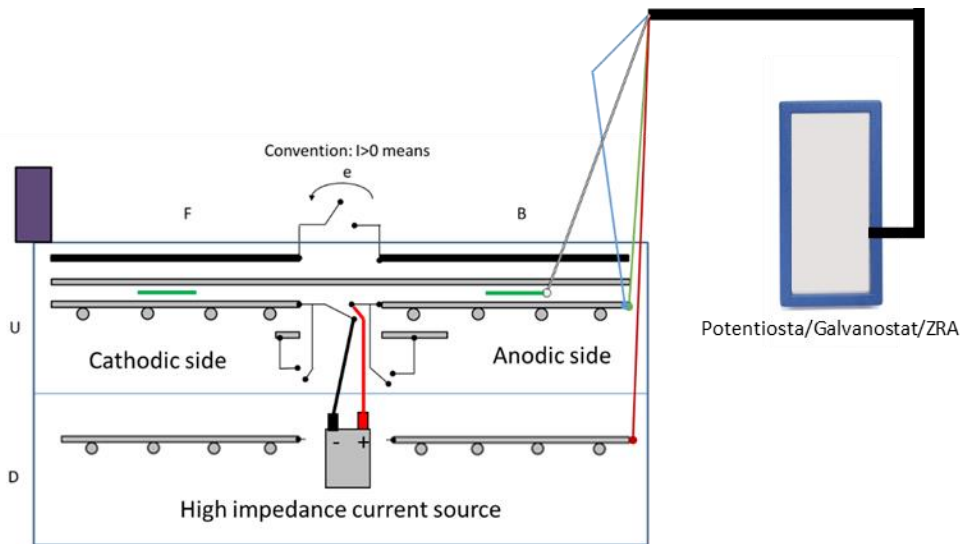


Figure 36. Schematic of connection for EIS tests.

Results:

In the following, potential evolution is presented for approximately the first 650 days of operation for boxes 1 and 2. Results for respectively duplicate boxes 3 and 4 were in general comparable. For the galvanized steel mesh specimens in box 1 (with cement-CLSM repair fill, Figure 37), potentials generally climbed towards nobler values, reaching between -0.6 V and -0.5 V vs. CSE after about 400 days. The potential evolution of the galvanized bar segments and galvanized steel meshes had a similar behavior, as expected since the galvanized segments are connected to their respective meshes. The continuous galvanized bars in each quadrant had potential evolution trends generally similar to those of the mesh and associated segments in each. The uncoated steel potential exhibited as expected a more positive potential than the galvanized components, and most positive in the CLSM octant, indicative of passivating conditions. In box 2 (polyurethane repair fill, Figure 38), potentials generally followed the same trend towards nobler values as in box 1. However, stabilization of potential occurred between -0.9 and -0.7 V vs CSE, values more negative than those seen in box 1. This is probably because no CLSM was present in box 2 that could potentially alter the backfill chemistry.

After commencing rainfall simulations, potential evolution of galvanized steel specimens in box 1 (cement-CLSM fill) (Figure 37) showed a slight drop in potential values. This is likely as a direct result of an increment in the water content of the backfill. Potentials of uncoated steel remained relatively unchanged, possibly due to growing steel oxides coating the bare steel as a result of corrosion activity over time. A comparable trend can be observed for box 3, duplicate of box 1.

Potential evolution of box 2, (polyurethane repair fill) (Figure 38) showed little change after rainfall simulations started, remaining relatively steady for all types of reinforcement.

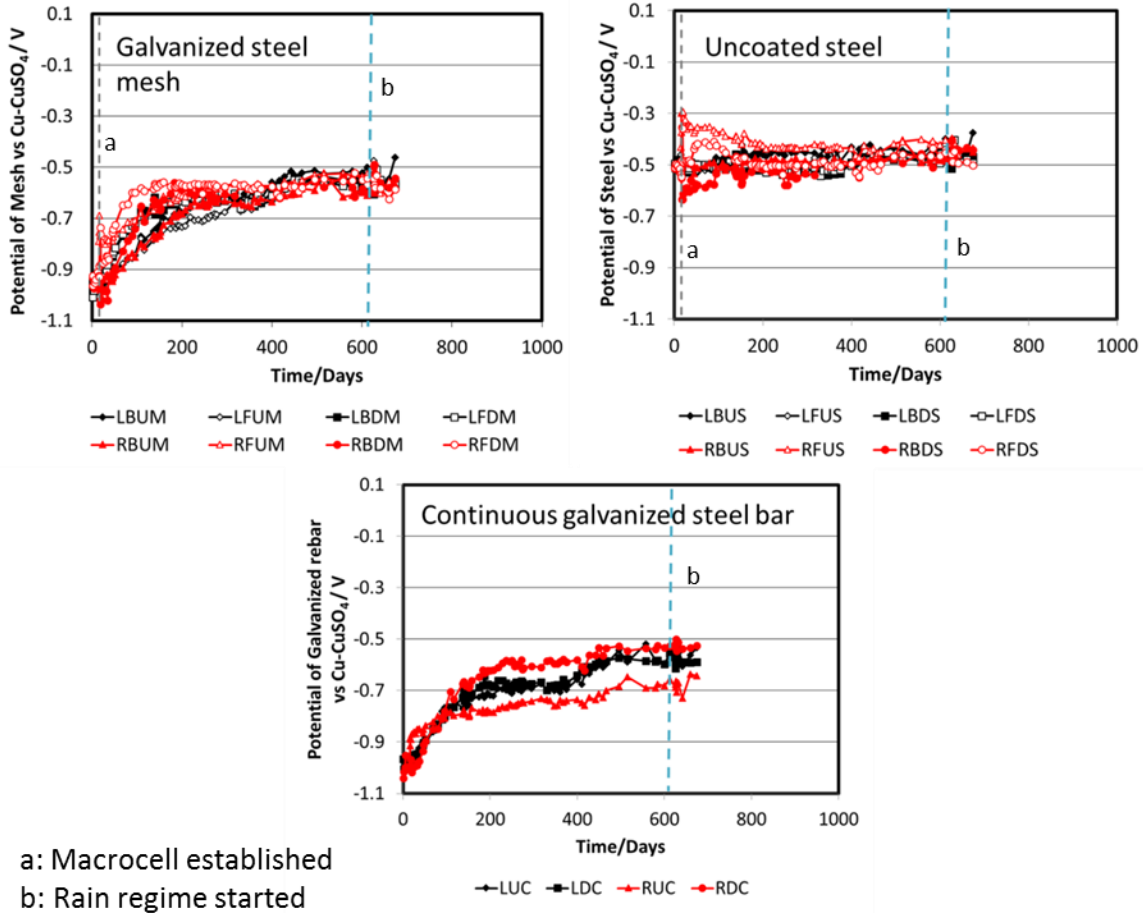


Figure 37. Potential (instant-off whenever applicable) evolution of electrodes in box 1 (with cement-CLSM repair fill). Red lines/markers correspond to right side (side with patch); black to left. Gray dashed line corresponds to the moment of establishing the macrocell by closing the connecting switch, and blue dashed line corresponds to the start of rain simulations.

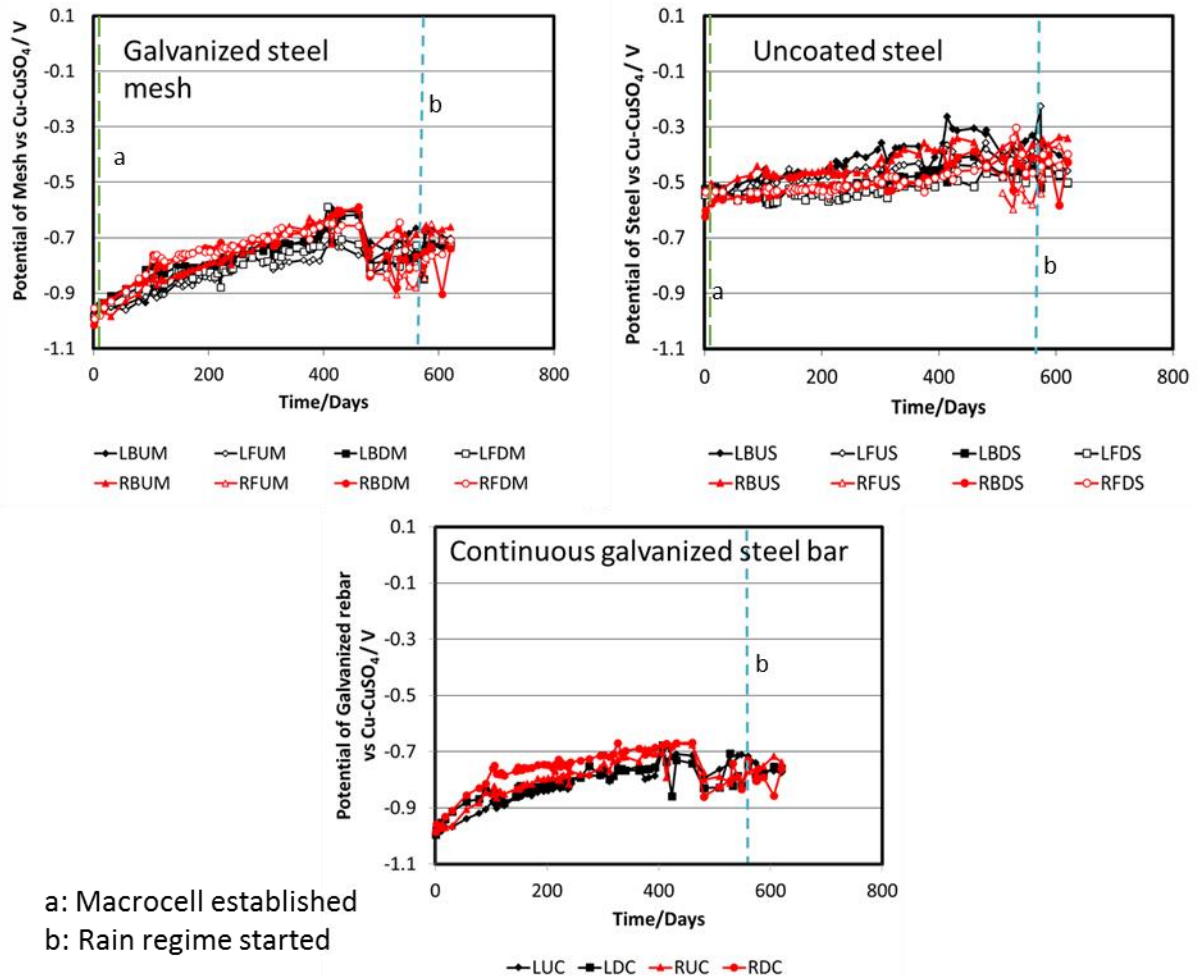


Figure 38. Potential (instant-off whenever applicable) evolution of electrodes in box 2 (with polyurethane repair fill). Red lines/markers correspond to right side (side with patch); black to left. Green dashed line corresponds to the moment of establishing the macrocell by closing the connecting switch when the repair material was delivered, and blue dashed line corresponds to the start of rain simulations.

Macrocell current evolution

Macrocell current evolution for the galvanized steel meshes is shown in Figure 39. In both boxes with CLSM repair fill (1 and 3) the mesh in the CLSM section (RFUM) was strongly cathodic with respect to the back mesh at the same level (RBUM). The latter experienced an initial anodic macrocell current in the order of 1-2 $\mu\text{A}/\text{cm}^2$, which is an overall aggravating effect comparable to that observed in the laboratory specimens. The effect decayed with time, but adverse galvanic coupling developed also for the galvanized mesh elements placed at the lower level on the same side. This effect, possibly caused by leachout from the upper region, was later on in the case of box 3 even stronger than that in the upper portion. On the left side of the boxes macrocell currents developed as well but of generally smaller magnitude, and in some

cases in the opposite direction of those in the right side. The causes for this behavior are under investigation but appear to be related to stray current coupling with the macrocells in the right side.

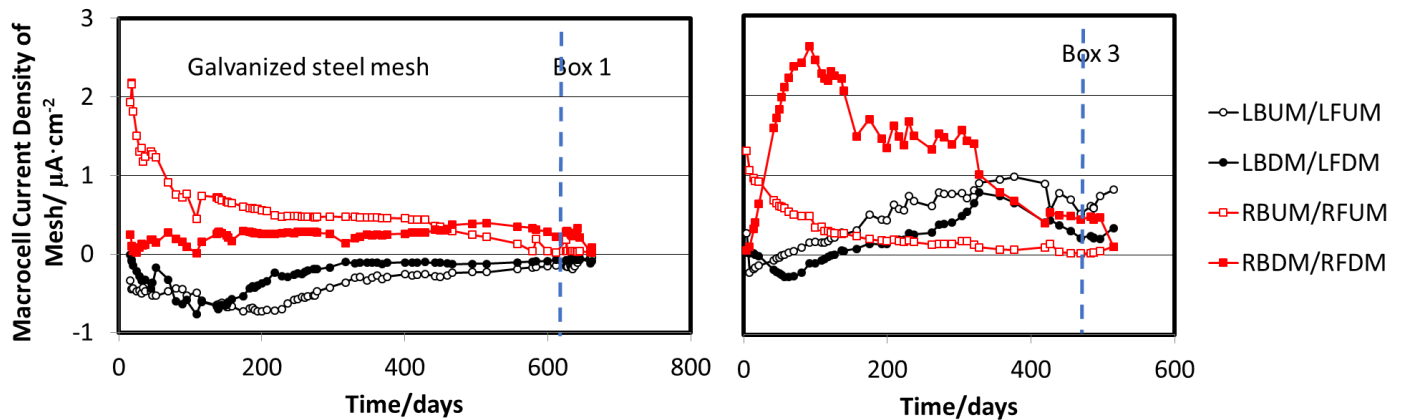


Figure 39. Macrocell current evolution for the galvanized steel meshes in duplicate boxes 1 and 3 with cement-CLSM repair fill. Positive values indicate the mesh in the back side is anodic. Blue dashed line corresponds to the start of rain simulations.

The short galvanized steel segments placed close to the front-back interfaces exhibited several instances of large macrocell current densities, as shown in Figure 40. The observed effect however was not largest at the expected position (RBUG/RBUM, the segment closest to the CLSM/backfill interface). Analysis of possible artifacts including effect of stray currents from the other macrocell couples will need to be examined in future investigations.

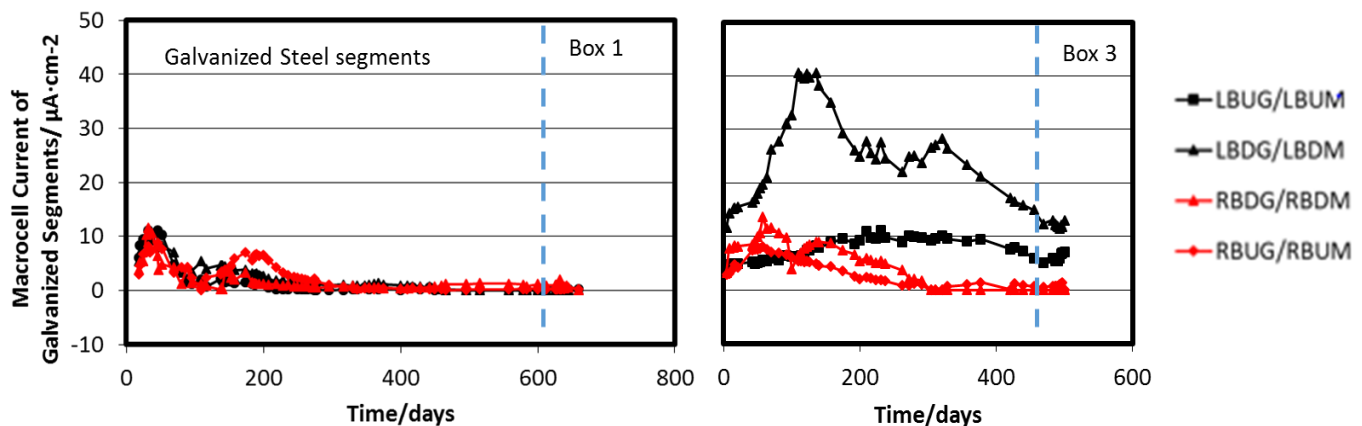


Figure 40. Macrocell current evolution for the galvanized steel wire segments on back side in duplicate boxes 1 and 3 with cement-CLSM repair fill. Positive values indicate segment is anodic. Blue dashed line corresponds to the start of rain simulations.

The uncoated steel bars in the quadrant containing the CLSM (Figure 41) showed as expected anodic behavior on the back side of that quadrant. Surprisingly, the bars in the

quadrant beneath it showed reverse macrocell polarity and much greater current density values. This behavior appears to be due to stray currents originating from the galvanized mesh array in the CLSM-backfill system immediately above.

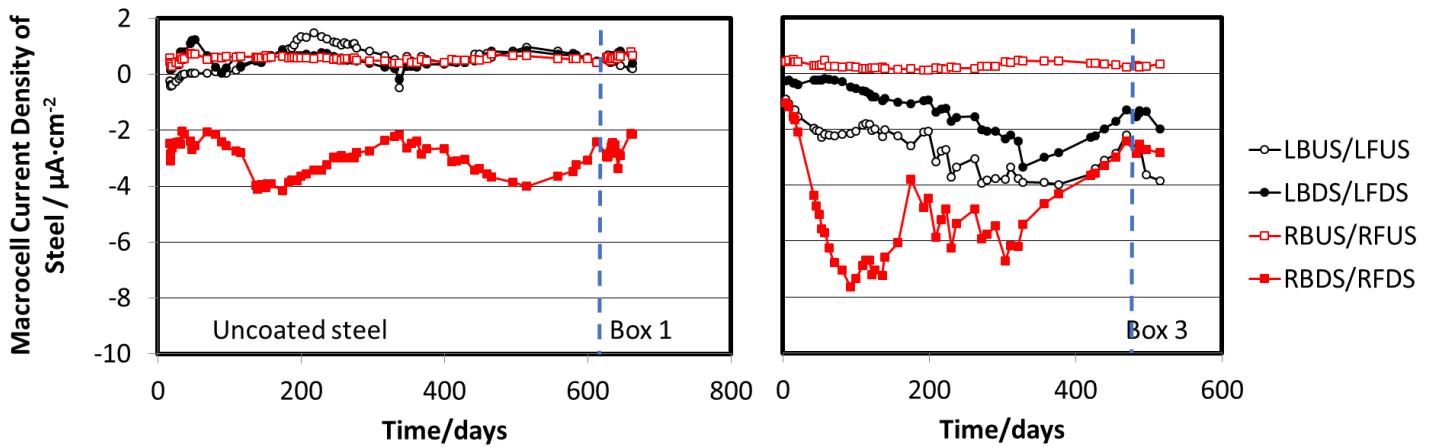


Figure 41. Macrocell current evolution for the uncoated steel bars in duplicate boxes 1 and 3 with cement-CLSM repair fill. Positive values indicate the mesh in the back side is anodic. Blue dashed line corresponds to the start of rain simulations.

Galvanized steel meshes in boxes 2 and 4 (Figure 42) (repair-filled with polyurethane grout) show very little sign of macrocell activity when compared with boxes 1 and 3 (cement-CLSM), consistent with small-scale experiments. Furthermore, the meshes in the other quadrants show very little macrocell action. This may be explained by noting that boxes 2 and 4 have no cementitious compound that could potentially affect the soil chemistry. Thus, from a corrosion control standpoint these results favor the use of polyurethane grout for fill repair applications.

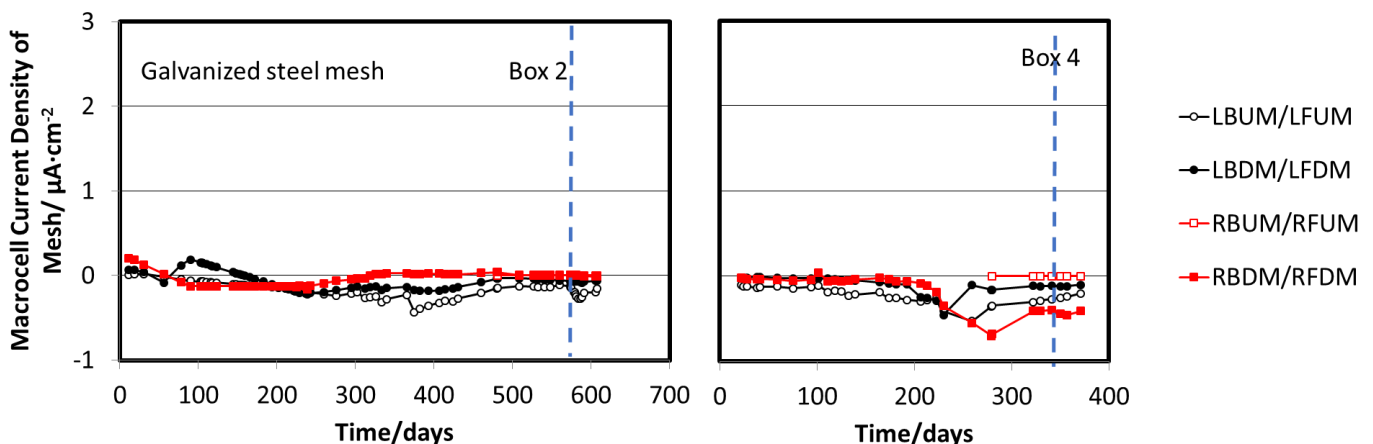


Figure 42. Macrocell current evolution for the galvanized steel meshes in duplicate boxes 2 and 4 with polyurethane repair fill. Positive values indicate the mesh in the back side is anodic. Blue dashed line corresponds to the start of rain simulations.

The short galvanized steel segments showed a slight macrocell action for the first 150 days in polyurethane repair fill box 2 and 250 days in duplicate box 4 (Figure 43), which then remained at near 0 $\mu\text{A}/\text{cm}^2$ afterwards. This is in contrast with the case for CLSM repair fill boxes 1 and 3, which showed a significantly higher macrocell activity that remains up to the latest measurement.

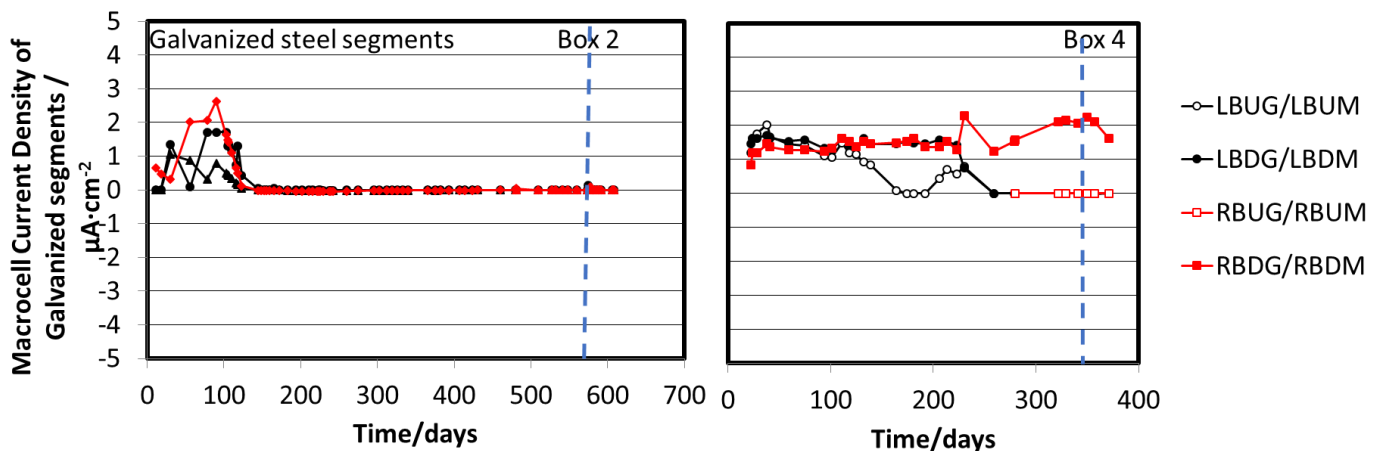


Figure 43. Macrocell current evolution for the galvanized steel wire segments on back side in duplicate boxes 2 and 4 with polyurethane repair fill. Positive values indicate segment is anodic. Blue dashed line corresponds to the start of rain simulations.

Bare steel in polyurethane repair fill boxes (Figure 44) showed signs of macrocell activity but only in the order of $\sim 1 \mu\text{A}/\text{cm}^2$, value that pales in comparison to those of CLSM repair fill boxes 1 and 3. These results further indicate that the use of polyurethane foam for void filling application minimize the macrocell activity of the system.

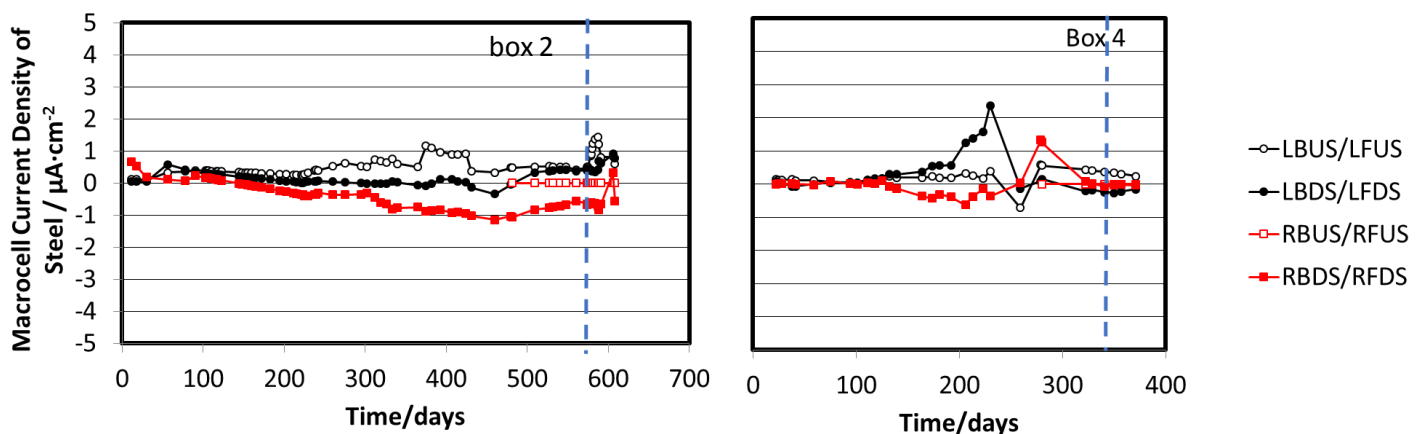


Figure 44. Macrocell current evolution for the uncoated steel bars in duplicate boxes 2 and 4 with polyurethane repair fill. Positive values indicate the mesh in the back side is anodic. Blue dashed line corresponds to the start of rain simulations.

Macrocell currents were also measured regularly after simulated rainfall started. In a period of 50 days, macrocell currents increased by about 10% and 30% in CLSM repair fill boxes 1 and 3 respectively. This observation is a possible indication of adverse effects whenever severe rain infiltrates the walls (e.g., during persistent rainstorms or hurricanes). Additionally, this situation may lead to increased leaching from the pore water of the CLSM patch to the soil, affecting the distribution of chemical species in the pore system and inducing macrocells in other regions within the wall. In contrast, polyurethane repair fill Boxes 2 and 4, did not show any noticeable detrimental effect from simulated rainfall, since the system macrocell currents either remained the same as before or even decrease slightly in some cases.

EIS results and corrosion aggravation estimates

Analysis of the impedance measurements in the large-scale boxes was considered to provide only nominal results due to observed large frequency dispersion of the data and uncertainty about the possible presence of a very long time constant component of the spectrum. Hence only a semiquantitative summary is provided here. Pending further analysis in future work, a simplified evaluation of the findings was conducted by computing the ratio of the ACR on the galvanized mesh at the backfill end of the box on the right side (the part that was coupled with the filled void, see Figure 31), to the ACR for the corresponding galvanized mesh on the left side (nominally no macrocell effect). The resulting ratio was 2.34 and 1.47 for boxes 1 and 3 respectively, with cementitious CLSM fill, and 1.43 and 1.28 for boxes 3 and 4 respectively, with polyurethane foam fill. Those values correspond to overall average apparent CAP values (see Section 2.2.1) $k \sim 1.9$ and $k \sim 1.35$ for the cement-CLSM and polyurethane conditions respectively. The order of the values is as expected (greater for cement-CLSM, nearer to unity for the polyurethane foam side) but it must be noted that any macrocell effect is averaged over the entire, large surface of the mesh, so those measurements do not capture much of the local corrosion enhancement that may be taking place near the fill/backfill interface.

Additional insight may be obtained by comparing the macrocell current densities of the short galvanized segments near the interface to those of the entire mesh. This comparison was made only for the cement-CLSM boxes where the macrocell currents were appreciable. The time-averaged segment/mesh macrocell current densities were ~ 5 and ~ 14 , respectively, for boxes 1 and 3 (for the first 632-day and 529-day periods, respectively) suggesting that an average value of $k \sim 10$ for the near-interface zone is prevalent for those systems.

2.2.3 Corrosion Modeling

Methodology

An exploratory corrosion distribution model was proposed and implemented by an idealization of an MSE Wall where reinforcing elements (in this case rod-like strips) are regularly distributed on a view from the outside of the wall (Figure 45 a). A square cross section unit portion of the MSE Wall, such that the wall could be reconstructed by combination of multiple identical unit portions, was then extracted as illustrated in Figure 45 b. Half of the unit was assumed to consist of a void filled with CLSM and the other half with normal backfill. The square cross section (Figure 46) was then approximated by a cylindrical symmetry section of equivalent cross sectional area. The reinforcing element was represented by a central rebar. A Finite Element Modeling (FEM) COMSOL Multiphysics ® platform was used to implement the calculations. The base case used parameters generally based on the laboratory experiment data presented earlier. A variation was performed to assess a different scenario, where the CLSM and backfill resistivity is 10 times greater than that found with the nearly saturated laboratory media, thus bracketing other possible realistic conditions. Figure 47 summarizes the ruling equations assumed for the system. Meaning of the symbols is indicated in the List of Symbols at the beginning of this report and in Table 4. The underlying assumptions are similar to those used in related modeling efforts for the corrosion of steel in concrete, and for brevity the description is deferred to material cited in the References section [28 ,29]. The anodic reaction in the CLSM media was assumed to proceed at a potential-independent rate with the indicated value, as a nominal representation of predominantly passive behavior there and with the understanding that more sophisticated expressions may be used in future implementations of the model. Table 4 lists the tentatively assumed model parameter values and sources additional to those just indicated. The medium-specific values were chosen to yield corrosion rates and potentials representative of those observed in the laboratory specimens generally toward the end of the first year of testing. It is emphasized that those choices are not intended as definitive descriptors for each case, but rather as a sampling of the variety of conditions and ways of quantifying behavior that may be used in this type of idealization. More representative values of those parameters of direct relevance to specific field conditions are expected to emerge as longer test times and additional information from large scale testing and field data become available.

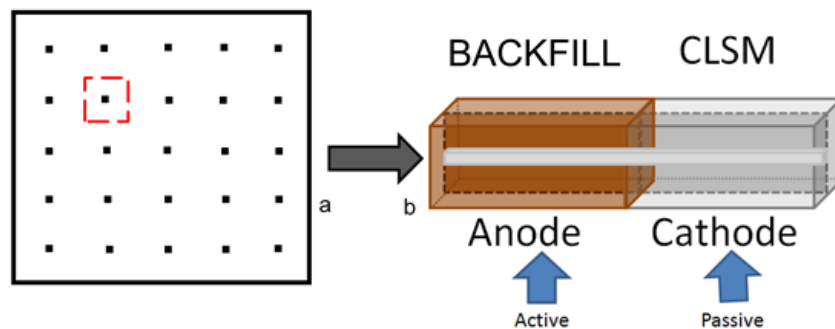


Figure 45. Rationale for the geometry used for model simulations.

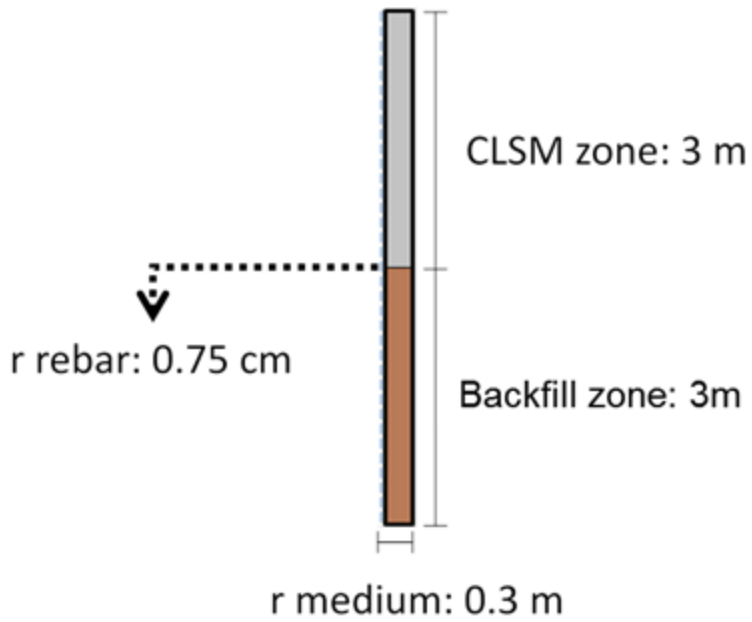


Figure 46. FEM domain geometry for model simulations. Rotational symmetry axis is located at the left.

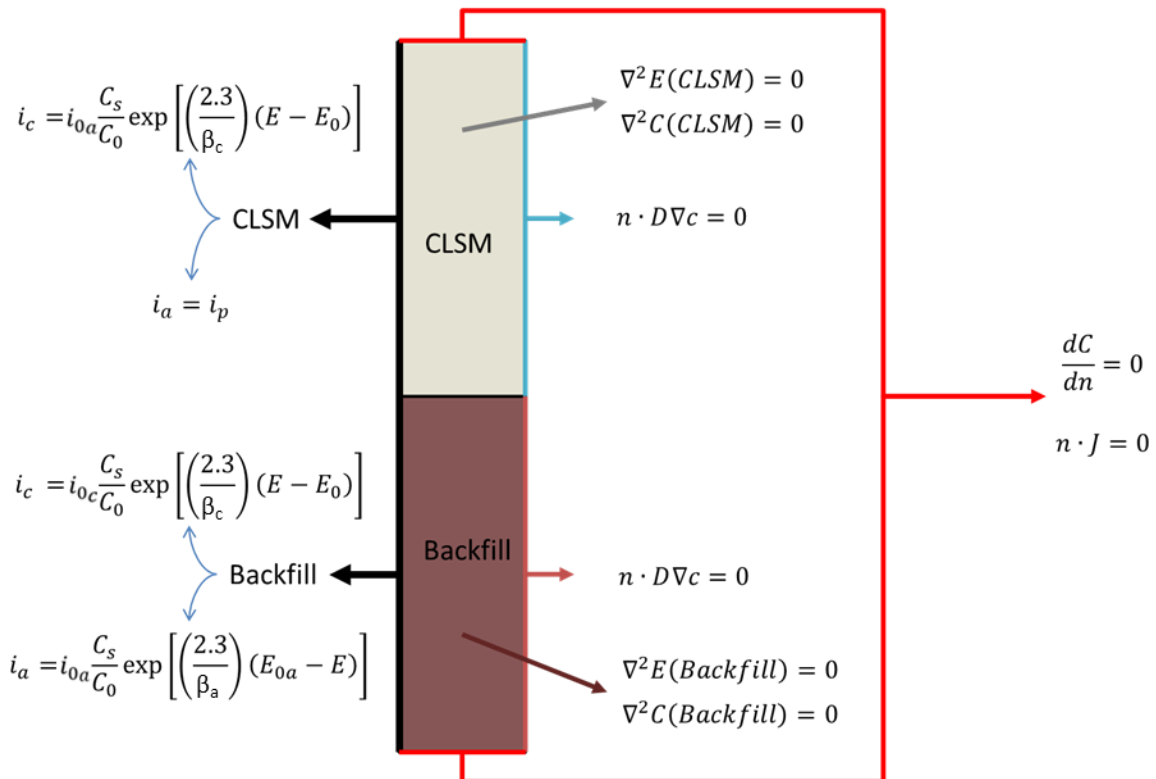


Figure 47. Ruling equations for model simulations.

Table 4. Parameters used for base case modeling simulation

| Parameter | Value | | Source |
|---|-------------------------------|----------------------|--|
| Radius of rebar (cm) | 0.75 | | Nominal value |
| Radius of cylinder representing the Medium (m) | 0.3 | | Nominal dimensions abstracted from Rossi [30] |
| Length of Cylinder (m) | 6 | | |
| Medium | Backfill | CLSM | Nominal values chosen to obtain polarization conditions similar to those inferred from EIS and open circuit potentials laboratory data |
| ρ (kohm-cm)* | 3; 30 | 3; 30 | |
| E_o , nominal cathodic equilibrium potential (V SCE) | 0 | | |
| E_o , nominal anodic equilibrium potential (V SCE) | -1 | | |
| i_{oc} , nominal cathodic exchange current density (A/cm ²) | 4x10 ⁻¹¹ | | |
| i_{oa} , nominal anodic exchange current density (A/cm ²) | 1.26x10 ⁻¹¹ | - | |
| D for Oxygen (cm ² /sec) | 1x10 ⁻⁴ | | |
| i_p , nominal passive anodic dissolution current density (A/cm ²) | - | 6.7x10 ⁻⁹ | Representative value based on EIS laboratory data |
| β , nominal Tafel slopes (V) | Anodic, 0.1 ; Cathodic, 0.135 | | Estimate abstracted from Peña [31] |

Results

As noted in the previously stated caveat, these results are presented mainly for insight on the processes involved, with more precise interpretation pending on the future availability of long term better established material-specific information. The conditions assumed resulted in a corrosion macrocell where the anodic portion corresponds to the metal embedded in the backfill (0 – 3 m), and the cathodic portion to the metal embedded in CLSM (3 – 6 m). Accordingly, the model output potentials are more negative for the backfill-embedded portion of the rod (Figure

48). This was expected, since the section in the CLSM was declared to be passive, while the active region was in the backfill. It is noted that when the resistivity increased by a factor of 10, the resulting potentials in the CLSM region were less negative, and those in the backfill less positive than in the base case. This too was as expected since the macrocell coupling decreased due to the higher effective circuit resistance

The plots of macrocell current density vs. position clearly show the distance effect [25, 29] (Figure 49) in agreement with the expectation that macrocell-induced corrosion is more aggressive near the backfill-CLSM interface. This is one of the characteristics of galvanic coupling corrosion [25], and the effect was sustained throughout the variations made in the model. Note the convention used whereby positive and negative current values represent anodic and cathodic currents respectively.

Figure 50 shows corrosion current density as a function of position in the anodic region (backfill-embedded steel). A marked increase in corrosion current density when nearing the backfill – CLSM interface was projected by the model. This implied as expected that this portion of the reinforcement near the interface is the one more susceptible to rapid loss of the galvanized film. The resistivity variation results indicate as expected that the zone of enhanced corrosion becomes narrower as the assumed resistivity increases [25].

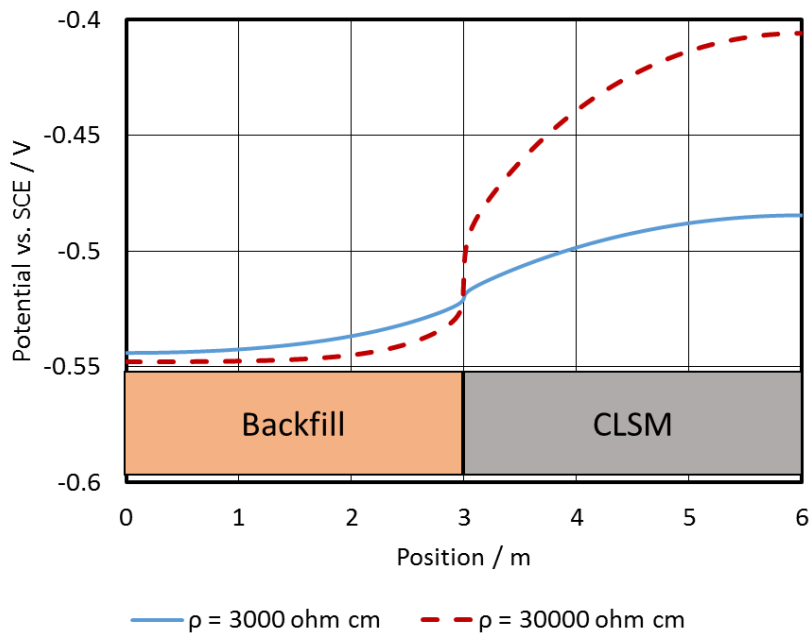


Figure 48. Corrosion potential vs. position in the reinforcement.

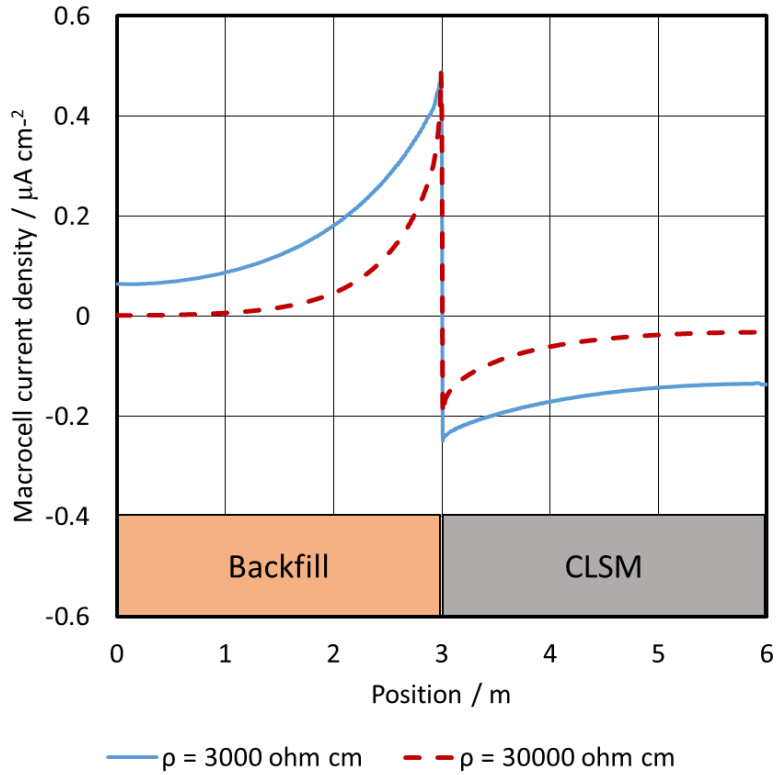


Figure 49. Macrocell current density vs. position in the reinforcement.

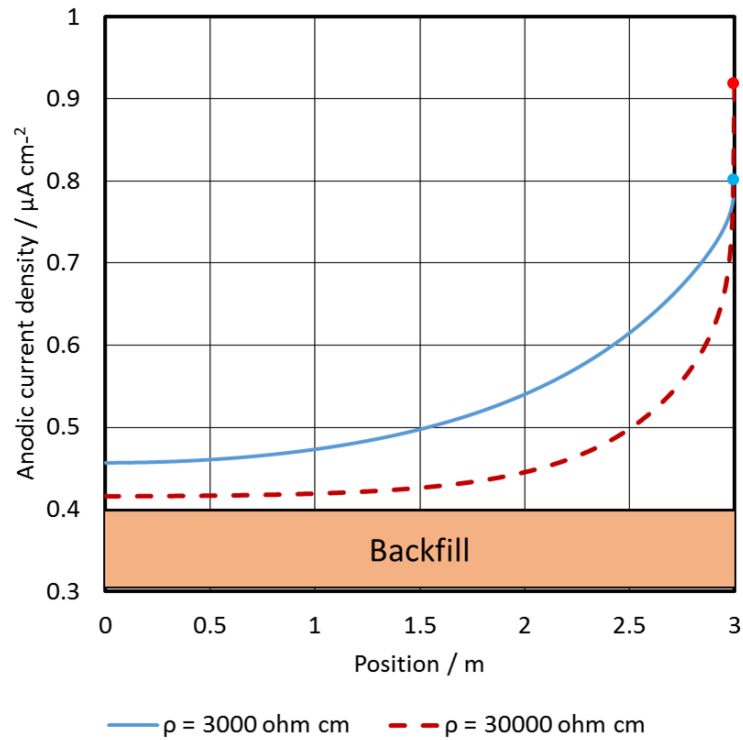


Figure 50. Corrosion current density vs. position (anodic portion).

The corrosion current densities in Figure 50, for points in the backfill far away from the junction and hence representative of uncoupled conditions, imply corrosion rates of about $6 \mu\text{m}/\text{y}$. This is, as expected, consistent with the rates estimated experimentally for freely corroding specimens, which were the basis of the model parameter choices. The result is roughly on the order of the often used nominal design estimate ($\sim 17 \mu\text{m}/\text{y}$ early on, dropping to $\sim 2 \mu\text{m}/\text{y}$ afterwards) for galvanized steel in MSE walls for the first 3 years of service [32]. The values of the projected macrocell current densities (Figure 49) were also in the order of magnitude of the values observed in the laboratory and large scale experiments. Near the interface and as a result of the macrocell coupling with the CLSM, the projected local corrosion rates for both the high and low resistivity variations examined became about twice as large as for the uncoupled condition. The adverse effect corresponds to a CAP value $k \sim 2$ for these model realizations. Other tentative model realizations to be confirmed by future work show greater values for k (e.g., ~ 3) when more severe conditions are assumed, such as a greater exchange current density for oxygen reduction on the CLSM side than on the backfill side. Overall, these results of exploratory scenarios highlight the possibility of significant adverse corrosion enhancement in these systems and indicate CAP values that are consistent with the experimental outcomes described in previous sections.

In additional calculations the model was modified (Figure 51) to explore the behavior when using the polyurethane void fill. Following the conditions discussed in the previous sections, it was assumed that a small layer of backfill (possibly mixed with corrosion products) would be left on the surface of the reinforcement after formation of the void. The layer thickness was assumed to be in the order of 1 mm, and for simplicity to have the same electrochemical properties as that of the bulk backfill. The steel in both sides of the interface is assumed to be in the active condition, as expected since the polyurethane is not assumed to have passivating properties in any residual interstitial water.

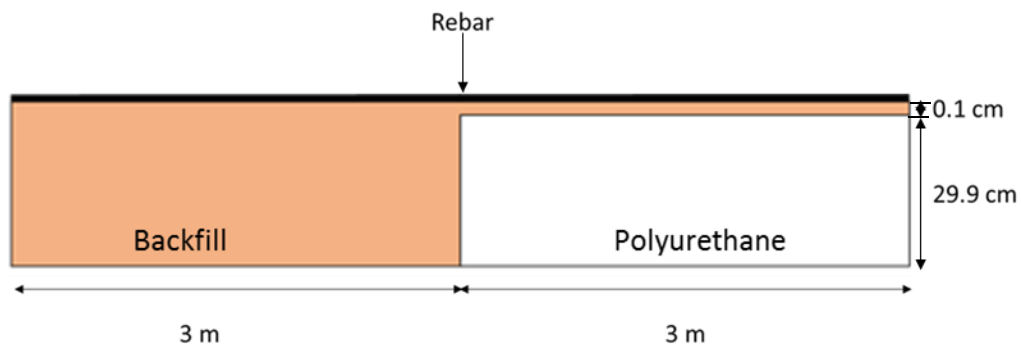


Figure 51. Model geometry for simulation with a void filled with polyurethane grout.

In contrast with the macrocell enhanced corrosion rates noted above for the CLSM scenarios, the cases for polyurethane show maximum macrocell current densities more than an order of magnitude smaller than those for the cementitious filler. This projection indicates promising performance for polyurethane, in agreement with both the laboratory and large scale experiment findings. That outcome is understood from the point of view of these exploratory calculations, which are focused on the potential adverse effect of macrocell formation on the reinforcement adjacent to the filled void. However, the polyurethane case brings up the alternative issue of possible adverse electrochemical effects within the filled void zone. As shown in Figure 52, the model projects a small but noticeable anodic macrocell action on the

reinforcement just inside the polyurethane boundary. That effect reflects the formation of a limited differential oxygen concentration cell, which is not expected to strongly enhance corrosion on the anode side as long as the reinforcement on the backfill side remains in the active condition (as assumed in the model). However, if a condition approaching passivity were to develop on the backfill side, a situation not unlike that of classic crevice corrosion could take place [25]. The possibility of events of that type, as well as the long term effects of moisture inside the interstice surrounding reinforcement inside polyurethane foam should be carefully investigated in follow up work. Direct examination of the polyurethane-embedded specimens in the laboratory and the large soil boxes after longer exposure times have been accrued may provide important additional information on this issue.

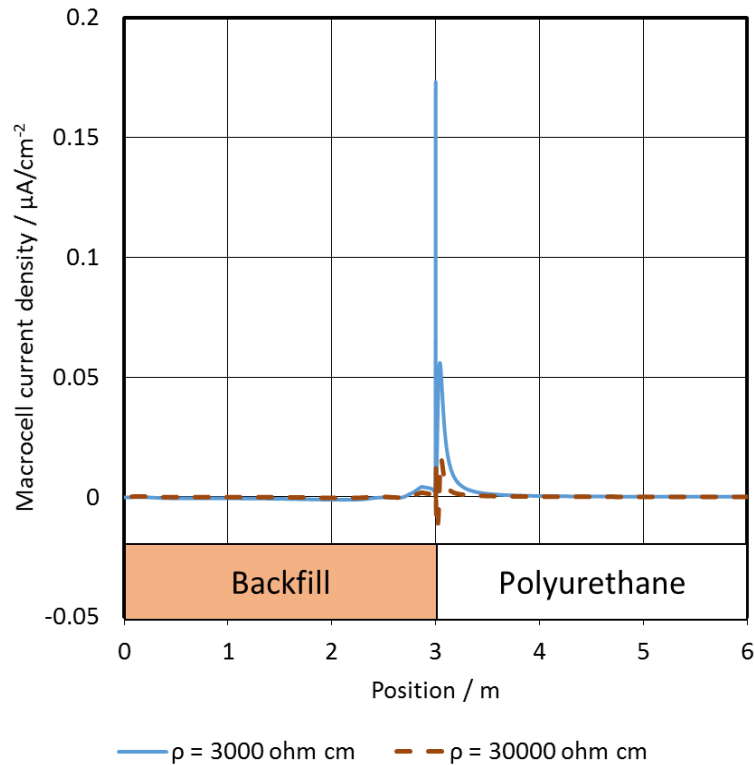


Figure 52. Macrocell current distribution for the polyurethane case. Compare with Figure 49 (thin vertical feature at 3 m is interpreted as a digitization artifact).

In summary, the exploratory corrosion distribution modeling further supports the expectation of increased corrosion on the backfill side of the CLSM-backfill interface, indicating values for the CAP in the order of $k \sim 2$ with the possibility of it becoming even higher under special conditions. The modeled effect is much smaller ($k \sim 1$) for the polyurethane void filler, with due attention to the possibility of other corrosion mechanisms becoming active in that case, as noted above.

2.2.4 Performance projection modeling

Baseline Case

The baseline statistical predictive model used here follows the treatment by Sagüés et al that was described in detail in previous publications [2, 3,33], so only salient points are addressed. For the baseline case a generic Florida MSE wall with no backfill voids is considered, containing a number of identical reinforcing elements, all embedded in the same kind of medium but with the understanding that variability in the medium and its condition causes corrosion rates to vary from element to element. The reinforcement consists of galvanized steel strips of width considerable larger than the thickness so that only the material loss perpendicular to the strip may be considered of importance. This geometric assumption is not limiting and the treatment could be easily converted to address circular wire reinforcement. Given the usual uncertainty in corrosion rate input parameters the mathematically simpler, flat strip model with thickness in the order of the wire radius will be used in the following as it provides comparable overall insight.

For further simplicity and also conservativeness, the corrosion rates are considered to be time-invariant as opposed to decreasing with time [34]. The time-invariant value is chosen to be representative of that corresponding to 10 yr age as evaluated from field observations [4,35] and as extrapolated from the laboratory data presented in sections 2.2.1 and 2.2.2.

The thicknesses of the galvanized layer on each side of the strip, and of the base steel are named g and s respectively, both expressed in μm . It is assumed that corrosion proceeds at the same rate on both sides of the strip in two consecutive stages, first consumption of the galvanized layer and then of the steel core. Based on earlier work [2, 3, 33, 35] and reflecting variability of medium and conditions the time-invariant corrosion rates, v (henceforth expressed in $\mu\text{m}/\text{y}$), are assumed to follow a statistical lognormal distribution, with parameters μ (\ln of the median value of $v \mu\text{m}^{-1} \text{y}$) and σ (standard deviation of $\ln(v \mu\text{m}^{-1} \text{y})$). In the following the corrosion rates for a given element will be named v_g and v_s respectively for those of the galvanized layer on each side of the strip and the plain steel (after it is exposed due to consumption of the galvanized layer). The respective cumulative distributions of values are designated as $C_g(v_g)$ and $C_s(v_s)$. For the assumed lognormal distribution those distributions functions are by definition

$$C(x) = \int_0^x \frac{1}{\sqrt{2\pi}\sigma z} e^{-\frac{(\ln(z)-\mu)^2}{2\sigma^2}} dz$$

Eq. 3

with C , σ and μ subscripted g or s for $x=v_g$ or v_s respectively (both expressed nondimensionally as their value in $\mu\text{m} \text{y}^{-1}$), and where z is an integration variable.

The corresponding probability distribution $P_g(v_g)$ for the corrosion rate of the galvanized layer is therefore:

$$P_g(v_g) = \frac{d(C_g(v_g))}{dv_g}$$

Eq. 4

The model considers a limit serviceability state corresponding to the condition whereby corrosion has progressed to the extent that the thickness of the strip steel core has lost ½ of its initial value (1/4 penetration from each surface). This choice results from the working assumption that a 50% loss of reinforcement thickness would likely significantly compromise structural function of the strip affected. The choice however is not critical to the viability of the model; it can be easily reformulated to reflect other metal loss limit states if future detailed structural analysis were to identify a more precise point to define local loss of structural integrity.

Per the above assumptions and as indicated in [2] the time to reach the limit state for a galvanized strip is given by

$$t_f = \frac{g}{v_g} + \frac{s}{4v_s} \quad \text{Eq. 5}$$

With those provisions the derivation by Sagüés et al [14] shows that

$$Ff(t) = \int_{V_g=g/t}^{\infty} P_g(V_g) \left(1 - C_s \left[\frac{s}{4} \left(t - \frac{g}{V_g} \right)^{-1} \right] \right) dV_g \quad \text{Eq. 6}$$

where $Ff(t)$, called the Damage Function, is the fraction of elements in the wall that reached the limit state by time t .

In the absence of repaired voids Eq. 7 provides a projection of cumulative future damage events in an MSE wall for the base case, with no filled voids. The overall serviceability limit state for the entire wall can then be expressed in terms of a given value for $Ff(t)$. For example, if structural calculations indicate that failure of 15% of the strips in a wall will render it unserviceable (e.g., the road supported by the wall would no longer be sufficiently supported and repairs are to be conducted before putting the structure back in service), then the age t at which $Ff(t) = 0.15$ is the projected end of the wall service life.

Effect of filled void presence

The following scheme is proposed for projecting the damage function for a wall containing voids which have been filled with a fill compound. For simplicity and conservativeness, it is assumed that the voids developed relatively early in the life of the structure, and that they were filled shortly afterwards; thus both void formation and fill are declared to occur at $t \sim 0$ y. The voids are assumed to be of a size such that they affect several reinforcing strips, but so that each strip is only affected by one void. Figure 53 shows a diagram proposing how to quantify the fraction of the total number of strips that is affected by filled voids. It is assumed that the ends of the horizontally placed strips are uniformly spaced on end on the front wall plane, with n_s strips per unit wall area. For a wall of total frontal area $A_T = w \cdot h$, the total number of strips is then $n_s \cdot A_T$. The voids are assumed to be present as shown in the figure, so each void of projected area A_i affects a number of strips $N_i = A_i \cdot n_s$. Hence, calling $A_v = \sum A_i$ the fraction of strips in the wall affected by void presence is simply given by

$$\alpha = A_v / A_T$$

Eq. 7

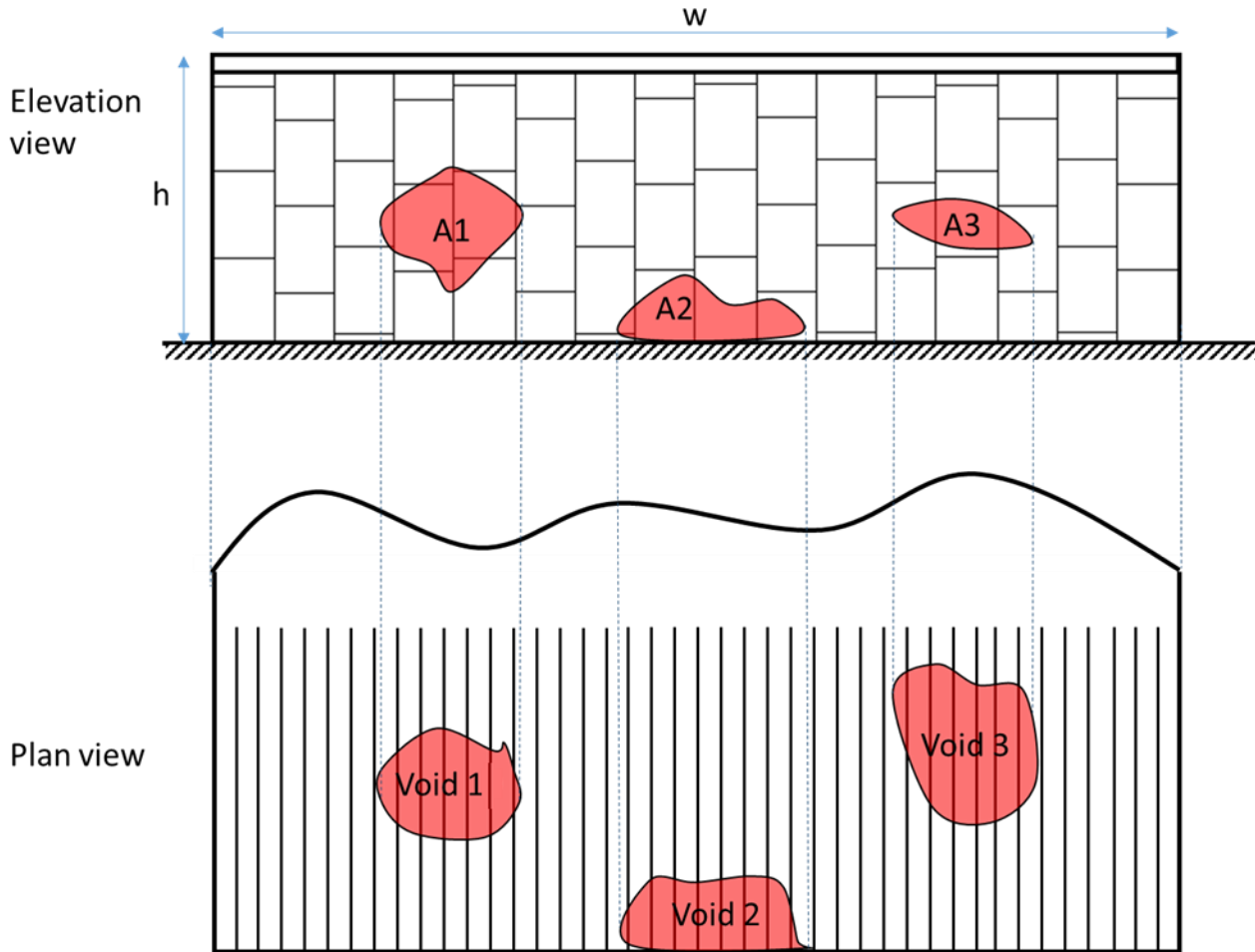


Figure 53. Schematic showing void distribution and effect on MSE wall reinforcement.

As shown in sections 2.2.1 - 2.2.3 the effect of a filled void on local corrosion rate at the filled void / backfill interface may be considered to be a local enhancement of the corrosion rates on the backfill side, respective to those in the void-free condition, by a CAP factor $k \geq 1$ so that $v_{gv} = kv_g$ and $v_{sv} = kv_s$ where the subscript v indicates the void-affected condition. In the following, the beneficial effect of any frictional force development for any section shorter than the original design length for reinforcing strips or wire mesh will be conservatively ignored. Hence, the reinforcing element serviceability limit for void-affected elements will be declared to be reached even if the steel cross section reduction to $\frac{1}{2}$ of the original value is localized to the small portion near the filled void / backfill interface.

With the above assumptions, the damage function for the entire wall can then be expressed as a combination of the damage evolving in the fraction $(1-\alpha)$ of the wall with sound, void-free soil which evolves as in the baseline case, and the void affected fraction α where localized corrosion rates of both galvanized layer and base steel are greater by a factor k. Hence the total projected damage function $F_f(t)$ for the structure can be expressed as:

$$F_{fr}(t) = (1-\alpha) F_f(t) + \alpha F_{fv}(t) \quad \text{Eq. 8}$$

where $F_{fv}(t)$ is the damage function for the void-affected region. The form of $F_{fv}(t)$ is the same as given in Eq. 5 for $F_f(t)$, but with v_{gv} instead of v_g , and with distribution functions C_{gv} (and P_{gv}) and C_{sv} instead of C_g (and P_g) and C_s respectively. As the factor k is assumed to be a flat multiplier over the void-free condition, the result on the function $F_{fv}(t)$ is that the void-affected condition lognormal parameters used to obtain the P_{gv} and C_{sv} distribution functions are now $\mu_{gv} = \mu_g + \ln(k)$ and $\mu_s = \mu_{sv} + \ln(k)$, while the lognormal standard deviations remain $\sigma_{gv} = \sigma_g$ and $\sigma_{sv} = \sigma_s$.

Cases examined

The base case consists of a generic MSE wall corresponding to the typical corrosion conditions determined during the 2009 survey of Florida structures under FDOT Project BD544-32 [3], for a selection of walls with galvanized elements with average age 16.0 y, and for plain steel probes embedded in some of the walls with average age 10.6 y. The corresponding parameters are listed in Table 5. Void-influence cases were examined per the parameters listed on Table 6, covering a number of plausible void incidence scenarios with α values corresponding to front wall void projections ranging from none, to very small (3 % of the wall surface) to extreme (100%). The corrosion aggravation parameter k was assigned alternative values ranging from 1.5 (mild) through 12 (very severe) bracketing a tentative value of $k=3$ as an approximate average of the sampling of values that were estimated from the results in Sections 2.2.1 - 2.2.3.

Table 5. Base case values abstracted from the BD544-32 survey [3] and assumed typical strip coating and steel thicknesses.

| Elements | Galvanized | Plain Steel |
|--|------------|-------------|
| Average Age (y) | 16.0 | 10.6 |
| Median corrosion rate per Lognormal Dist. ($\mu\text{m}/\text{y}$) | 0.64 | 4.65 |
| $\mu (\ln(v_{\text{median}} \mu\text{m}^{-1} \text{y}))$ | -0.45 | 1.54 |
| σ | 0.29 | 0.693 |
| Coating (one-sided) or steel (full) thickness (μm) | 150 | 4000 |

Table 6. Scenario parameters investigated

| |
|--|
| Corrosion aggravation parameter: $k= 1$ (base case) 1.5, 3, 6, 12 |
| Void incidence parameter: $\alpha=0.03, 0.1, 0.3$ and 1 (entire wall affected by voids), corresponding to 3%, 10%, 30% and 100% incidence. |

As in the initial modeling approach [2,3], a baseline localized corrosion concentration factor = 2 (effectively multiplying the median values by 2 and increasing μ accordingly over the values in Table 5) was assumed as well, to capture the effects of non-uniform soil conditions and to compensate for possible non-conservativeness in the other modeling assumptions. The value of k acts as a compounding factor on that base multiplier. The resulting modeling projections are shown in Figure 54.

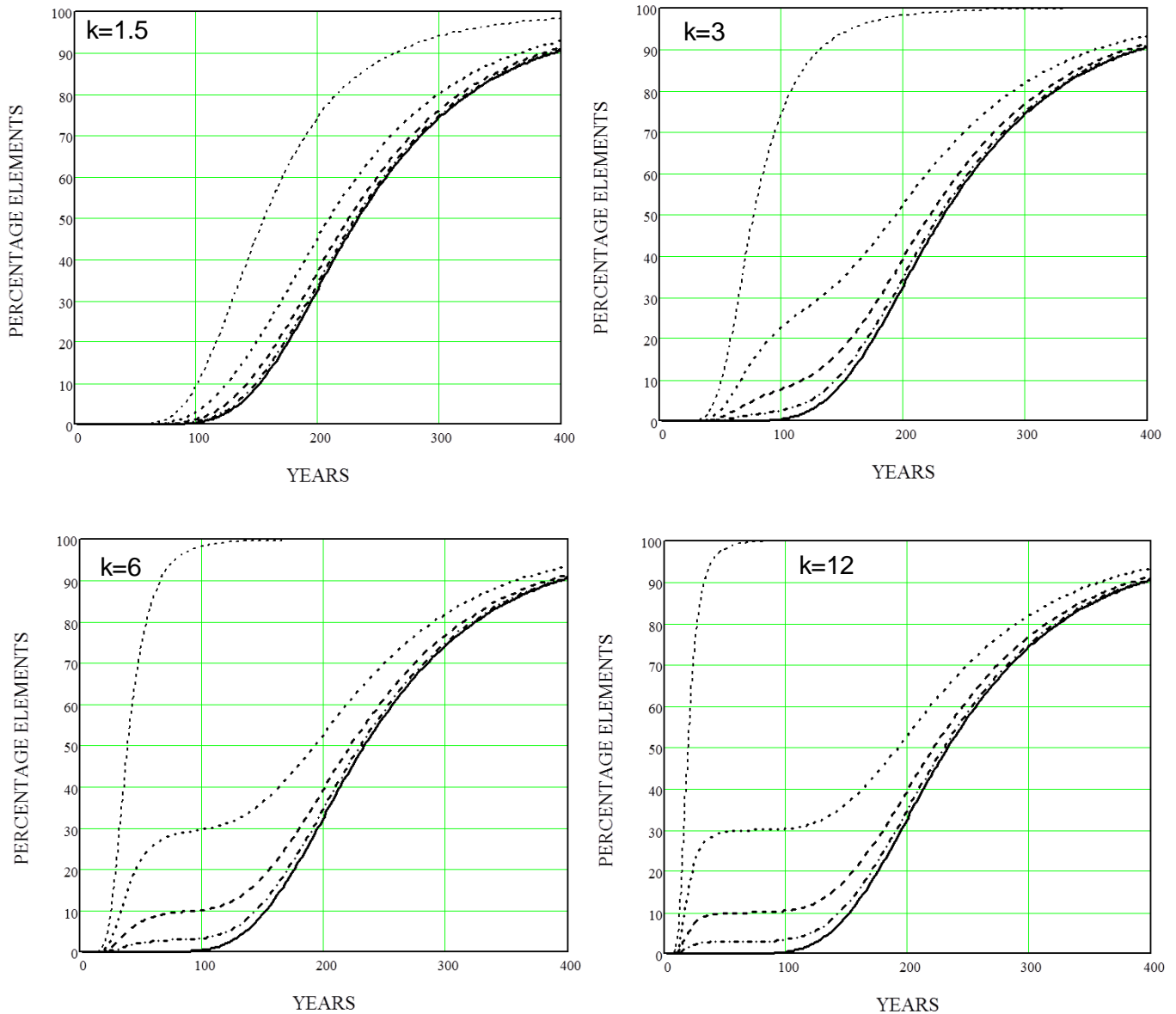


Figure 54. Modeling projections showing damage function as percentage of reinforcing elements having reached their limit state at the structure age indicated. Solid line corresponds to the base case (no voids). Each family of cases corresponds to the indicated corrosion aggravation parameter k . Broken lines to the left of the base case indicate progressively greater void incidence parameters corresponding to 3%, 10%, 30%, and 100% of all elements affected by repaired voids.

It is emphasized that the model projections are primarily for insight on possible consequences of repair choices, and are not intended as a design tool. The modeling approach used involves sweeping assumptions and conservative as well as non-conservative simplifications, subject to refinement in future implementation. An example of such refinement is introduction of the effect of variability of g and s , which was ignored in the present model as a non-conservative simplification. The model projections should always be contrasted with available evidence of performance as revealed by future surveys and experimental results.

With the above caveats, it is noted that the base case (solid lines in Figure 54) reproduces the projections indicated in Ref. [3], where no adverse effect of voids was considered. The projected damage percentage for such system is virtually nil until ~ 100 yr age, reflecting the conditions encountered in earlier FDOT MSE wall surveys.

The projections for cases where there are filled voids cover a wide range of possible conditions, but based on the experimental and corrosion distribution modeling findings the scenarios for $k=3$ would appear to be the most representative of the use of a cement- or slag-based CLSM void filler. For such scenarios and a small CLSM-filled void incidence (3%) the damage projection is near nil up to about 50 yr, and reaches only about 2% at a typical 75 yr design service life. Projected damage becomes increasingly severe as the assumed void incidence increases. If the fill-induced corrosion aggravation were less important (e.g., $k=1.5$, which is in the order of the lower end of the values observed in the experiments), the projected tolerance to CLSM-filled void presence becomes proportionally greater, with nearly nil damage at 75 years except in extreme void incidence cases. The cases with $k=6$ and $k=12$ are presented for completeness, covering scenarios where extreme localized corrosion were to occur. In general, the information in Figure 54 should be examined by contrasting the projected damage with a plausible limit state, as determined by consideration of the structural implications of losing the function of a given number of reinforcing elements.

From a corrosion aggravation standpoint, the results to date for the polyurethane fill would correspond to $k\sim 1$, so for that filler the model as formulated does not project damage beyond that of the base case. It is noted that the model is limited to corrosion projections and does not consider any issues on the mechanical performance of the straps when embedded in foam, such as possible loss of frictional force compared with regular backfill. Those issues and potential related drawbacks require separate consideration beyond the scope of this project. Furthermore, the extent of testing to date has not evaluated any long-term effects of moisture-related corrosion on the foam-embedded reinforcement or of possible crevice corrosion development there as noted in Section 2.2.3. Such potentially adverse effects should require further assessment in future investigations.

3 RECOMMENDATIONS

The project findings confirmed the expectation that the use of conventional cementitious CLSM void filler materials carries a risk of added reinforcement corrosion at the CLSM/backfill interface. A quantitative estimate of the effect of that corrosion has been developed for several possible scenarios. Keeping in mind that those projections are subject to considerable uncertainty, it is nevertheless recommended that the outcomes of those scenarios be examined by structural experts for the following: First, to assess which limit state values are best descriptors, from the point of view of reinforcement cross section loss (the model uses 50% as a tentative value) as well as percentage of reinforcing elements (the value of the damage function) reaching that loss level, to indicate that serviceability has ended. Criteria can depend on elevation of the part of the structure affected, and should be formulated in a way suitable for integration with procedures used by the Department in earth wall design. Second, once the appropriate limit states are identified, to examine the typical actual extent of filled void incidence (parameter α) that may be expected for the FDOT structures inventory, and apply that information to determine to what extent a 75 year design service life may be achieved under those conditions given the most plausible CAP value (e.g., $k \sim 3$) and for the other alternative k values evaluated. That exercise will assist in revealing to what extent and promptness, if any, a transition toward alternative filler materials is in order.

Should the above analysis indicate that a transition to alternative fillers is highly desirable, the present investigation findings on materials performance provide relevant information. Results have shown that the alternative slag or MgO-based filler materials may not provide a substantial advantage, from the standpoint of corrosion control, over the conventional cementitious CLSM. From the tests conducted here, the polyurethane foam filler remains as an attractive alternative to avoid macrocell corrosion formation. Hence, contingent on its having adequate structural performance from a mechanical standpoint, that material is recommended for further consideration. However, extended corrosion testing should be conducted to assess risk of corrosion at the polyurethane filler - reinforcement interface.

4 CONCLUSIONS

1. Corrosion activity of the galvanized steel reinforcement was found to be enhanced by a macrocell current resulting from the simultaneous presence of Controlled Low-Strength Material (CLSM) and backfill. The enhancement was observed, as expected, on the backfill side.
2. Laboratory experiments indicated that macrocell coupling could substantially increase the corrosion of the galvanized coating in the backfill side of a void repair with CLSM based on cement or on slag. The modestly lower pH of the latter did not appear to be a sufficiently beneficial factor in lowering the extent of adverse macrocell action. CLSM based on MgO, although having a pH closer to neutral, still resulted in significant adverse macrocell corrosion development.
3. Large-scale experiments provided confirming indications that substantial adverse macrocell enhancement of corrosion could take place on the backfill side of a cement CLSM repair.
4. Large-scale experiments showed also indication that leachout from the cementitious CLSM repair could induce significant macrocell action in adjacent reinforcement. The implications of this effect need to be further investigated.
5. Consistent with the experimental results, a computer model also indicated that the corrosion rate of the parts of the reinforcement closest to the CLSM/backfill interface could be significantly greater (e.g., 2 times or more) than the average rate along the reinforcement in the backfill side, indicative of further aggravation at the interface region.
6. Small and large-scale experiments using a polyurethane foam void fill confirmed the expectation of much lower tendency for macrocell aggravation of corrosion in the backfill side.
7. Performance modeling projections quantified the amount of corrosion related MSE wall degradation that may be expected as the structure ages. The projected deterioration for a typical design service life goal age was near nil for moderate void incidence and macrocell corrosion aggravation near the low end of the values observed experimentally. Appreciable deterioration, to be contrasted with structurally relevant limit states, was projected for other possible regimes.
8. It is recommended that the performance model projections be analyzed via structural considerations for choice of representative limit state, to establish to what extent a transition to an alternative void filler material is desirable. If such transition is needed, the use of polyurethane foam is recommended for further consideration and evaluation. However, extended corrosion testing should be conducted to assess risk of corrosion at the polyurethane filler - reinforcement interface.

5 REFERENCES

1. National Highway Institute Office of Bridge Technology. (2001) *Mechanically Stabilized Earth Walls and Reinforced Soil Slopes Design & Construction Guidelines* (Report FHWA-NHI-00-043). Washington, D.C.: U.S. Department of Transportation.
2. Sagüés, A.A., Scott, R., Rossi, J., Peña, J., and Powers, R. (2000) "Corrosion of Galvanized Strips in Florida Reinforced Earth Walls." *ASCE's Journal of Materials in Civil Engineering*, Vol. 12, pp. 220-227.
3. Berke B.S., and Sagüés, A.A. (2009) *Update on Condition of Reinforced Earthwall Straps*. (Florida Department of Transportation Report BD544-32). Tampa, FL: University of South Florida..
4. Florida Department of Transportation (2012) *Standard Specifications for Road and Bridge Construction*. Tallahassee, FL.
5. Hitch, J. L. (1998) "Test Methods for Controlled Low-Strength Material (CLSM): Past, Present, and Future," *The Design and Application of Controlled Low-Strength Materials (Flowable Fill)*, ASTM STP 1331, A. K. Howard, and J. L. Hitch, Eds., American Society for Testing and Materials.
6. Folliard, K.J. (2006) *Corrosion study and implementation plan for NCHRP*. (Report 597). Washington, D.C.: National Cooperative Highway Research Program.
7. Folliard, K.J., Du, L., Trejo, D., Halmen, C., Sabol, S., and Leshchinsky, D. (2008) *Development of a Recommended Practice for Use of Controlled Low-Strength Material in Highway Construction NCHRP*. (Report 597). Washington. D.C.: National Cooperative Highway Research Program.
8. Trejo, D., Halmen, C., Folliard, K.J., and Du, L. (2005) "Corrosion of Metallic Pipe in Controlled Low-Strength Materials—Parts 1 and 2." *ACI Materials Journal*, Vol. 102, pp. 192-201.
9. Trejo, D., Halmen, C., Folliard, K.J., and Du, L. (2005) "Corrosion of Metallic Materials in Controlled Low-Strength Materials—Part 3." *ACI Materials Journal*, Vol. 102, pp. 429-437.
10. Halmen, C., Trejo, D., Folliard, K.J., and Du, L. (2006) "Corrosion of Metallic Materials in Controlled Low-Strength Materials—Part 4." *ACI Materials Journal*, Vol. 103, pp. 53-59.
11. Iyengar, S. R., and Al-Tabbaa, A. (2007) "Developmental Study of a Low-pH Magnesium Phosphate cement for Environmental Applications". *Environmental Technology*. Vol. 28, pp. 1387-1401.
12. Bodi, J., Bodi, Z., Scucka, J., and Martinec, P. (2012) "Polyurethane Grouting Technologies". In *Polyurethane*, Fahmina Zafar and Eram Sharmin, eds. Rijeka, Croatia: InTech.
13. Pons, F., Landwermeyer J.S., and Kerns L. (1998) "Development of Engineering properties for regular and quick-set flowable fill." *The Design and Application of Controlled Low-Strength Materials (Flowable Fill)*, ASTM STP 1331, A.K. Howard and J.L Hitch, Eds. American Society for Testing and Materials.

14. Najafi, F., Tia, M., Lovencin, W., Javed, A., Chaudry, H., and Abbas, A. (2004) *Use of Accelerated Flowable Fill in Pavement Section* (Florida Department of Transportation Project BC354-53). Gainesville, FL: University of Florida.
15. City of Cleveland, Office of the Mayor. (Undated). *Flowable Fill aka "Cleveland LSM": Specification for Utility Trenches*. Cleveland, OH: City of Cleveland.
16. Taha, R.A., Alnuaimi, A.S., Al-Jabri, K.S., and Al-Harthy, A.S. (2007) "Evaluation of controlled low strength materials containing industrial by-products". *Building and Environment*. Vol. 42, pp. 3366–3372.
17. Passe, P.D. (2012) *Mechanically Stabilized Earth Wall Inspector's Handbook*. Florida Department of Transportation. Tallahassee, FL.
18. Cáseres, L., Sagüés, A.A., Kranc S.C., and Weyers, R.E. (2006) "In situ leaching method for determination of chloride in concrete pore water". *Cement and Concrete Research*. Vol. 36, pp. 492-503.
19. Sagüés, A.A., Moreno, E.I., and Andrade, C. (1997) "Evolution of pH during in-situ leaching in small concrete cavities". *Cement and Concrete Research*. Vol. 27, pp. 1747-1759.
20. Li, L., Sagüés A.A., and Poor N. (1999) "In situ leaching investigation of pH and nitrite concentration in concrete solution". *Cement and Concrete Research* Vol. 29, pp. 315-321.
21. Florida Department of Transportation. (2000) *Florida Method of Test for pH of Soil and Water*. Designation: FM 5-550. Tallahassee, FL.
22. Sagüés, A.A., Kranc S.C., and Moreno, E.I. (1998) "An Improved Method for Polarization Resistance from Small Amplitude Potentiodynamic Scans in Concrete". *Corrosion*, Vol. 54, p.20-28.
23. Paz Velásquez, E. A., and Sagüés, A. A. (2014) "High Frequency Impedance Dispersion of Corroding Galvanized Steel in Soils", Presentation No. 485, 225th Meeting of The Electrochemical Society, Orlando, FL.
24. Stern, M., and Geary A.L. (1957) "Electrochemical Polarization I. A theoretical analysis of the shape of polarization curves". *Journal of Electrochemical Society*. Vol. 104, pp. 56-63.
25. Jones, D.A. (1995) *Principles and prevention of corrosion*. Prentice Hall. 2nd edition.
26. Yeomans, S.R. (2004) *Galvanized steel reinforcement in concrete*. Elsevier. 1st edition.
27. U.S. Climate Data for Tallahassee, FL.:<http://www.usclimatedata.com/climate/florida/united-states/3179>
28. Sagüés, A.A., Sánchez, A.N., Lau, K., and Kranc, S.C. (2014) "Service Life Forecasting For Reinforced Concrete Incorporating Potential-Dependent Chloride Threshold", *Corrosion*, Vol. 70, pp. 942-957.
29. Kranc, S.C., and Sagüés, A.A. (1994) "Computation of Reinforcing Steel Corrosion Distribution in Concrete Marine Bridge Substructures". *Corrosion*, Vol. 50, pp. 50-61.

30. Rossi, J. (1996) "The Corrosion Behavior of Galvanized Steel in Mechanically Stabilized Earth Wall Structures" M.S Thesis. College of Engineering. Department of Civil and Environmental Engineering, University of South Florida.
31. Peña, J.A. (1994) "Seawater Contamination and Soil Gradation Effect on Corrosion of Galvanized Steel Strips in Reinforced Earth Walls", M.S. Thesis, College of Engineering. Department of Civil and Environmental Engineering, University of South Florida.
32. AASHTO. (2004) *LRFD Highway Bridge Design Specifications*. American Association of State Highway and Transportation Officials, Washington, D.C., Third Edition.
33. Berke, B.S., and Sagüés, A.A. (2008) "Long term corrosion performance of soil reinforcement in Mechanically Stabilized Earth Walls". Paper No. 08319, Corrosion 2008, NACE International, Houston, TX.
34. Elias, V. (1990) *Durability/Corrosion of soil reinforced structures*. (Report No. FHWA-RD-89-186). Washington, D.C.
35. Sagüés, A.A., Rossi, J., Scott, R.J., Peña, J., Simmons, T. (1998) *Influence of corrosive inundation on the corrosion rates of galvanized tie strips in mechanically stabilized earth walls*. (Florida Department of Transportation Report , Job No. 99700-3531-119, WPI 0510686). Tampa, FL: University of South Florida.